ChemComm

HIGHLIGHT

View Article Online
View Journal | View Issue

Cite this: *Chem. Commun.*, 2025, **61**, 17254

Data-driven atomistic modeling of crystalline and glassy solid-state electrolytes

Rui Zhou, Kun Luo and Qi An *

All-solid-state batteries promise safer, more stable, and higher-energy-density storage, but progress hinges on atomistic insight into solid electrolytes. Machine-learning force fields (ML-FFs) offer near-first-principles accuracy at molecular-dynamics scales, enabling simulations that are orders of magnitude larger and longer than *ab initio* approaches (*e.g.* density funcitonal theory). In this Review, we discuss recent ML-FF frameworks and the application of them on studying both crystalline and glassy solid electrolytes. Particually, we compare various ML-FF models and training strategies, examine transferability and uncertainty quantification, and outline best practices for data generation and validation. The applications of ML-FF on battery systems reveal advances in illustrating ionic-transport pathways, defect-mediated conduction, structure–property relationships, phase stability and transformations, and interfacial phenomena at grain boundaries and electrode|electrolyte contacts. Then we conclude with perspectives on key challenges—including long-range electrostatics, chemical reactivity, and multi-component complexity. Together, these developments position ML-FFs to accelerate the discovery and optimization of robust, high-performance solid electrolytes for practical all-solid-state batteries.

Received 26th August 2025,
Accepted 1st October 2025

DOI: 10.1039/d5cc04921k

rsc.li/chemcomm

1. Introduction

Global decarbonization and electrification are driving a sharp rise in battery demand.[1] Conventional lithium-ion batteries with flammable liquid electrolytes face safety risks and energy density limits that restrict their broader deployment. All-solid-state batteries (ASSBs) have been proposed to address these challenges with enhanced safety and higher energy density potential.[2] However, broad commercialization of ASSBs has yet to be realized due to challenges in cost, cycle life, and fast charging.[3] Many of these barriers are fundamentally rooted in materials issues—most notably the solid-state electrolyte (SSE), which strongly impacts the battery system's safety, power capability and durability. Despite the long commercial success of liquid electrolytes, practical SSEs are hindered by limited ionic conductivity, unstable and resistive electrode–electrolyte interfacial, and manufacturing scalability constraints.[4]

To address the materials limitations outlined above, we need tools that resolve the atomistic processes governing ionic transport and interfacial stability. Computational methods now play an important role in advancing the understanding and design of battery materials,[5–8] particularly for investigating phenomena that are difficult to access experimentally.[9]

Department of Materials Science and Engineering, Iowa State University, Ames, Iowa 50011, USA. E-mail: qan@iastate.edu

Rui Zhou

Rui Zhou is a PhD student under supervision of Prof. Qi An at Iowa State University. His research focuses on the computational design and discovery of novel solid electrolytes.

Kun Luo

Kun Luo received his bachelor's degree from Wuhan University of Science and Technology in 2010 and his PhD from Yanshan University in 2017. He is now a postdoctoral scholar at Iowa State University. His research centers on investigating the atomic mechanisms of structural changes in materials to comprehend their novel properties.

Meanwhile, machine learning approaches are accelerating discovery and optimization across battery materials research.[10–13] Among these, machine learning force fields (ML-FFs) have emerged as a powerful computational framework applied broadly to inorganic SSEs systems from crystalline phases to glassy solid state electrolytes (GSEs).[13–16] ML-FFs bridge the long-standing fidelity-efficiency gap in materials simulation: classical force fields are fast but constrained by fixed functional forms and empirical parameterization,[17,18] which limits accuracy for multicomponent SSEs chemistries and their complex ion transport. This transportation is often mediated by a wide range of defects, including stacking faults,[19] Li-stuffing,[20] cation site disorder,[21,22] and anion site disorder.[23–25] First-principles calculations (*e.g.* density functional theory, DFT) offer high accuracy, but their computational cost scales drastically with system size ($O(N^3)$–$O(N^7)$ in the number of electrons), restricting accessible time-scales and length-scales. In contrast, ML-FFs enable simulations that reach millions of atoms,[26] and extend into microsecond regime while retaining near-DFT accuracy, making them ideal for examining long-timescale ionic transport in batteries.

In this Review, we will first discuss the major families of inorganic solid-state electrolytes and their transport and stability characteristics. Then, we summarize recent computational studies that employed ML-FFs to investigate SSE structures, ionic dynamics and electrode–electrolyte interfaces. Finally, we will present case studies illustrating how to use ML-FFs to elucidate ionic transport mechanisms, quantify interfacial processes, and map structure–property relationships, thereby informing the design of next-generation ASSBs.

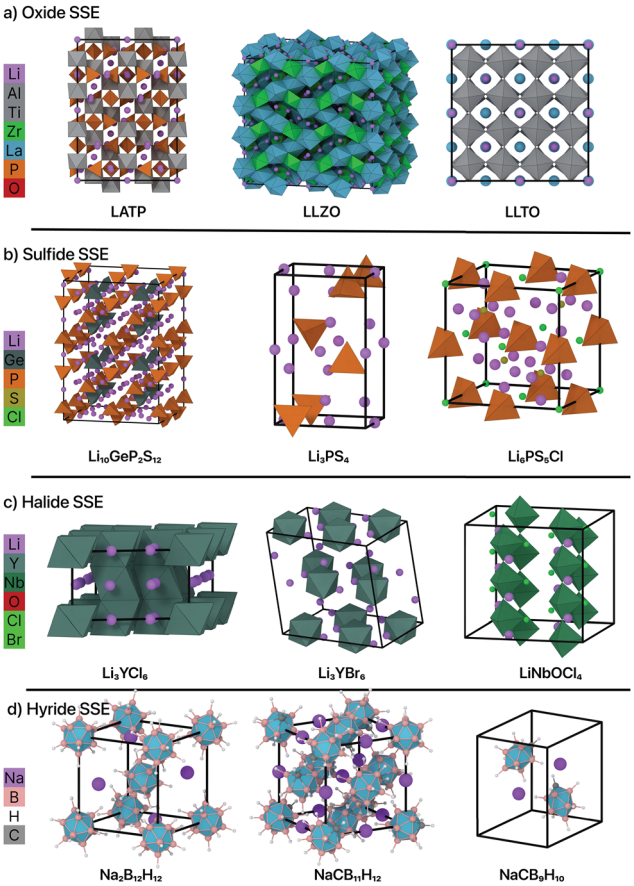

Fig. 1 Schematic structures of representative crystalline solid-state electrolytes (SSEs): (a), oxides; (b), sulfides; (c), halides; (d), hydrides. For clarity, anions at the vertices of the coordination polyhedra (O, S, and halides) are omitted.

2. Solid state electrolytes

Based on different criteria, SSEs can be categorized into several classification schemes. Structurally, they are commonly grouped into crystalline SSEs, amorphous glassy solid-state electrolytes, and glass-ceramic SSEs. Fig. 1 shows structural schematics of typical crystalline SSEs, including oxides, sulfides, halides, and hydrides. Certain crystalline SSEs, such as lithium germanium phosphorus sulfide (LGPS), achieve a high room-temperature ionic conductivity of 12 mS cm^{-1}, but their macroscopic performance can be limited by grain boundaries resistance and anisotropy.[27] In contrast, GSEs are intrinsically isotropic and free of grain boundaries.[28] The ionic conductivity of a GSE is theoretically higher than that of its crystalline counterpart because of its typically larger molar volume.[29] In certain systems, such as NASICON-type,[30] sulfide-based,[31] and halide-based electrolytes,[32] an even higher ionic conductivity can be achieved through partial crystallization of the amorphous precursor into a glass–ceramic solid electrolyte. This enhancement arises from the formation of highly conductive nanoparticles and grain-boundaries.[33] The resulting glass–ceramic solid electrolyte combines the favorable mechanical properties of the flexible polyanion network found in glasses with the enhanced ionic conductivity provided by the crystalline parts.

In addition to the crystalline–amorphous distinction, SSE can be classified by the topology of their anion framework.[34] In polyhedral-network types SSE, polyhedral share corners or edges to form a continuous framework, that provides migration channels for Li^+, Na^+ transportation. In cluster-anion electrolytes, the anions arrange into fcc, hcp, or bcc sublattices

Qi An

Qi An has been an Associate Professor in the Department of Materials Science and Engineering at Iowa State University since 2022. His research primarily focuses on elucidating the processing and properties of materials—such as batteries, semiconductors and ceramics—through advanced computational approaches including machine learning, electronic structure calculations, and atomistic simulations.

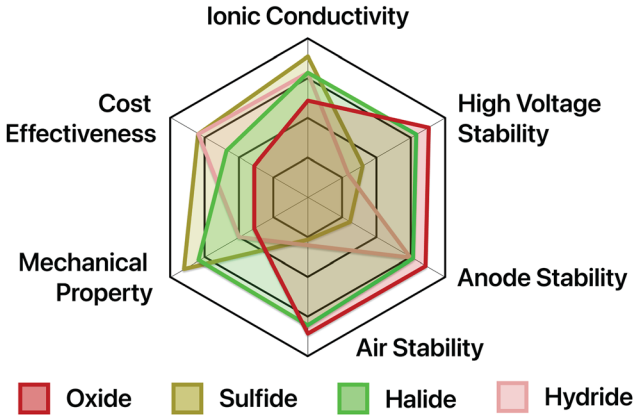

Fig. 2 Radar chart that compares the key performance of various types of solid electrolytes.

without direct interconnection between them, and alkali cations diffuse through interstitial sites.[34]

From a compositional perspective, SSEs are categorized into oxides, sulfides, halides, and hydrides, as shown in Fig. 2. Oxides electrolytes (Fig. 1(a)) generally exhibit good compatibility with metal anodes and wide electrochemical windows, but they typically possess low ionic conductivity, higher stiffness, and often require high-temperature processing.[27,35] Sulfides (Fig. 1(b)) often exhibit high room-temperature ionic conductivity and enable low-temperature processing, yet they suffer from narrower electrochemical stability windows, reactivity with metal anodes, and sensitivity to air and moisture.[36,37] Halides electrolytes (Fig. 1(c)) provide wide electrochemical windows,[38,39] and have shown encouraging cycling performance. For example, the recently reported $LaCl_3$-based LiTaLaCl SSE show 81.6% capacity retention after 100 cycles against a Li metal anode.[40] Complex hydrides (Fig. 1(d)) show good thermal and electrochemical stability and favorable mechanical properties, but they are sensitive to moisture and electrode materials.[41]

In what follows, we focus on representative Li-based SSEs with high ionic conductivity to illustrate these classes and to establish structure–property links that guide materials selection and device design.

2.1 Crystalline solid-state electrolytes

Garnet type. Garnet-type SSE with the general formular $Li_xM_3M'_2O_{12}$ are among the most intensively studied oxide systems. They are structurally related to the oxide-garnet framework of $Ca_3Al_2(SiO_4)_3$, with Li replacing the Si atoms and occupying interstitial sites within the garnet lattice. Depending on the Li content x, garnet-type SSEs are often divided into subtypes: Li_3-type ($Li_3La_3Te_2O_{12}$, $Li_3Ln_3Te_2O_{12}$), Li_5-type ($Li_5La_3M_2O_{12}$), Li_6-type ($Li_6ALa_2M_2O_{12}$), and Li_7-type ($Li_7La_3Zr_2O_{12}$).[27]

Among these, $Li_7La_3Zr_2O_{12}$ (LLZO) is the prototypical oxide SSEs, achieving room temperature ionic conductivity up to 10^{-3} S cm^{-1} in optimized compositions. LLZO exists in two polymorphs: a high-conductivity cubic phase[42] and a low-conductivity tetragonal phase.[43] In the tetrahedral structure, Li ordering—including full occupation of tetrahedral sites—reduces the number of available vacancies and narrows migration pathways, yielding conductivities near 10^{-6} S cm^{-1}. In contrast, the cubic phase features partially occupied Li sublattices that create a three-dimensional network of accessible sites, enabling less correlated Li^+ motion and substantially higher conductivity.[34,44]

Perovskite type. Typical perovskite-type SSEs, most notably the $Li_{3x}La_{2/3-x}TiO_3$ (LLTO) family and compounds of the form (Li, Sr)(M, M′)O_3, are derived from the ABO_3 perovskite structure, in which large A-site cations (*e.g.* La^{3+}, Sr^{2+}) and smaller B-site cation (*e.g.*, Ti^{4+}, Zr^{4+}) define the framework for fast-ion conduction.

Perovskite-type SSEs are generally A-site deficient, creating vacant A sites that enable Li^+ migration through the interconnected BO_6 octahedral channels.[45] Tetragonal LLTO attains room-temperature ionic conductivities on the order of 10^{-4} S cm^{-1}, with optimal compositions around x = 0.11, achieving 1.3 × 10^{-3} S cm^{-1}.[46] In LLTO, La^{3+} cations are unevenly distributed along the *c*-axis, resulting in La-rich and La-poor layers. Li^+ ions migrate relatively freely within the *ab* plane, whereas transport along the *c*-axis is limited by temperature-dependent bottlenecks associated with this La ordering.

NASICON type. The NASICON (Na superionic conductors) family was first reported in 1976 with the general formula $Na_{1+x}Zr_2Si_xP_{3-x}O_{12}$.[47] Lithium-based NASICON-type SSEs adopt the formula $LiMM'(PO_4)_3$ and typically exhibit room-temperature ionic conductivities of 10^{-4} to 10^{-3} S cm^{-1}. A prototypical member is $Li_{1+x}Al_xTi_{2-x}(PO_4)_3$ (LATP), for which optimal Al substitution (x = 0.3) yields conductivities near ~10^{-3} S cm^{-1} at room temperature.[48]

In NASICON-type SSEs, MO_6 octahedra connect with PO_4 tetrahedra through corner-sharing oxygen atoms, forming a 3D framework that facilitates alkali ion movement in LATP, aliovalent Al^{3+} substitution for Ti^{4+} requires charge compensation by additional Li^+, creating preferred Li interstitial sites adjacent to AlO_6 units. Although the smaller Al^{3+} contracts the lattice, the combined effects of increased charge carrier concentration and favorable local environments enhance Li^+ mobility and boost conductivity.[48–50]

LGPS type. The earliest LISICON (Li superionic conductor) materials, such as $Li_{14}Zn(GeO_4)_4$, exhibited low room-temperature ionic conductivity (~10^{-4} mS cm^{-1}).[51] Replacing oxygen with sulfur led to thio-LISICON compositions (*e.g.* $Li_{3.25}Ge_{0.25}P_{0.75}S_4$) that improved conductivity into the 10^{-4} to 10^{-3} S cm^{-1} range.[52,53]

The $Li_{10}GeP_2S_{12}$ (LGPS) family, first reported in 2011, achieves exceptional room-temperature conductivity of up to 12 mS cm^{-1}.[54–56] Unlike the orthorhombic thio-LISICON structures, LGPS adopts a $P4_2/nmc$ tetragonal structure[54] consisting of a three-dimensional framework comprising $(Ge_{0.5}P_{0.5})S_4$ tetrahedra, PS_4 tetrahedra, along with LiS_4 tetrahedra, and LiS_6 octahedra. Li^+ transport proceeds through quasi-one-dimensional channels along the c axis that are interconnected

within the ab plane, yielding effectively three-dimensional diffusion pathways.[57]

Argyrodite type. The original argyrodite Li_7PS_6 exhibits low room-temperature ionic conductivity (10^{-6} S cm^{-1}) because its high-conductivity cubic phase is only stable at elevated temperatures (*e.g.* 483 K).[58] Deiseroth and co-workers overcame this limitation by substituting one sulfur with a halide X (Cl, Br, I) in the chemical unit to form Li_6PS_5X, thereby stabilizing the high-temperature cubic phase at room temperature and achieving conductivities on the order of 10^{-3} S cm^{-1}.[59] Subsequent studies showed that additional cation substitutions (*e.g.* Si, Ge) can likewise stabilize the cubic phase and other high temperature phases at ambient conditions.[60]

Li_6PS_5X argyrodite-type SSEs adopts a crystal structure with space group of $F4\bar{3}m$. The anions framework forms a cubic close-packed sublattice in which PS_4 tetrahedra occupy octahedral sites, while remaining S^{2-} anions reside in tetrahedral sites. Li^+ primarily occupies the 24g and 48h Wyckoff positions.[59,61] For Cl and Br compositions, S^{2-} and halide anions exhibit site disorder over the 4a and 4c positions. This anion disorder and Cl^--induced Li^+ vacancy formation has been identified as a key contributor to the enhanced Li^+ conductivity of argyrodite electrolytes.[24,25,62,63]

Halide type. Halide-type SSEs generally have the chemical formula Li_aMX_b and can be categorized by metal center into group 3 elements (*e.g.* Y, Sc, Er), group 13 elements (*e.g.* Al, Ga, In), and divalent metals.[38] Many group 3 and group 13 metal halides reach room-temperature ionic conductivities on the order of 10^{-3} S cm^{-1}.

In Li_3YCl_6 and Li_3YBr_6, the halide anions form close-packed sublattices (hexagonal close-packed (HCP) for Li_3YCl_6 and cubic close-packed (CCP) for Li_3YBr_6), while Li^+ and Y^{3+} cations occupy octahedral sites. The high ionic conductivity is attributed to partially vacant octahedral sites that provide interconnected diffusion pathways. Owing to its HCP stacking, Li_3YCl_6 exhibits strongly anisotropic diffusion: concerted Li^+ migration along the c axis dominates overall conductivity because it proceeds with lower activation barriers than diffusion in the ab plane.

LNCO type. Oxyhalide SSEs are an emerging class that seek to combine the chemical stability of oxides with the high Li^+ mobility often found in halides. The anti-perovskite structure Li_3OCl oxyhalide reaches room-temperature conductivities of $\sim 10^{-4}$ S cm^{-1}. More recently, metal oxyhalides have shown markedly higher performance: Hu *et al.* reported a low-cost LiZrClO oxyhalide SSE with a room temperature conductivity of 2.42 mS cm^{-1},[64] and the studies on $LiNbOCl_4$ (LNCO) and $LiTaOCl_4$ demonstrated ionic conductivities near 10^{-2} S cm^{-1} at room temperature.[65] Their sodium counterparts can also achieve high ionic conductivities on the order of 10^{-3} S cm^{-1}.[66]

Despite these promising transport properties, the crystal structure of $LiNbOCl_4$ remains under activate debate[65,67–69] due to poor crystallinity and low coherence length.[67] Regardless, it is commonly described as consisting 1D parallel polyanion chains built from $[NbOCl_4]^-$ octahedra, with highly disordered Li^+ ions occupying interstitial sites.[68,69] Li^+ transport involves two different diffusion pathways: (1) diffusion along the *a*-axis following the polyhedral chain; and (2) diffusion within the bc plane, with the former mechanism generally considered energetically favored.[69]

Complex hydrides. Motivated by the discovery that $LiBH_4$ exhibits high Li^+ conduction and can function as a solid-state electrolyte, complex hydrides have emerged as a distinct SSE family. These materials are composed of alkali and alkaline-earth cations (*e.g.* Li^+, Na^+, Ca^{2+}) and complex anions such as BH_4^-, AlH_4^-, and *closo*-type borate/carborate species ($B_{12}H_{12}^{2-}$, $B_{10}H_{10}^{2-}$, $CB_9H_{10}^-$, $CB_{11}H_{12}^-$).

These materials typically exhibit ordered low-temperature phases and disordered (often "plastic") high-temperature phases, the latter displaying substantially higher ionic conductivity. For example, $Li_2B_{12}H_{12}$ undergoes an order–disorder phase transition at $\sim$615 K; in the disordered phase, rotationally mobile $B_{12}H_{12}^{2-}$ anions occupy the fcc sublattices while Li^+ migrates through vacancy-rich interstitial networks. Because these highly conducting disordered phases are typically unstable at room temperature, compositional strategies such as anion mixing[70–72] have been employed to stabilize them closer to practical operating conditions. In systems including $NaCB_{11}H_{12}$–$NaCB_9H_{10}$ and $Na_2B_{12}H_{12}$–$Na_2B_{10}H_{10}$ anion mixing has successfully suppress the order–disorder transition temperature and preserved fast-ion transport at reduced temperatures.[71]

2.2 Glassy solid-state electrolytes

GSEs offer unique advantages due to their amorphous structure, lower elastic moduli that mitigate stress during volume changes under charge/discharge cycles, inherent isotropic ionic conduction, the absence of grain boundaries and thus grain-boundary resistance, and superior mechanical compliance.[73] Their grain-boundary-free microstructure also inhibits dendrite nucleation and growth, addressing a key failure mode of many crystalline electrolytes.[74]

Theoretically, GSEs can achieve a higher ionic conductivity than their crystalline counterparts because structural disorder provides greater free volume and less constrained diffusion pathways. In addition, the absence of grain boundaries eliminates intergranular impedance that commonly limits performance in polycrystalline solids.

Thiophosphate glass. Li_2S–P_2S_5 (LPS) glasses are among the most widely studied GSEs. The $75Li_2S{\cdot}25P_2S_5$ composition exhibits a room-temperature ionic conductivity of $\sim 2 \times 10^{-4}$ S cm^{-1} with a Li^+ transport number near unity.[75]

Despite these advantages, LPS glass suffers from poor compatibility with Li anodes due to interfacial chemical reactivity. Several modifications strategies have been developed to address this limitation. Introducing a second network formers, such as Si, improves cycling stability by suppressing dendrite formation.[28,76] In addition, SnS_2 additions enhance the air stability.[76] Furthermore, halide additions, particularly LiI, significantly enhance conductivity; for example, adding 20 mol% LiI to $70Li_2S{\cdot}30P_2S_5$ increases conductivity from 1.3×10^{-4} to 5.6×10^{-4} S cm^{-1} and widens the electrochemical

stability window.[77] Oxygen doping offers another route and typically improves chemical stability.[78]

LiPON glass. Lithium phosphate oxynitride (LiPON) is another important family of the GSEs, typically achieving conductivities of $\sim 10^{-6}$ S cm^{-1},[79] which limits its application primarily to thin film batteries. Despite its lower conductivity relative to other systems, LiPON shows exceptional stability against Li metal, sustaining over 10 000 cycles with 95% capacity retention. This stability makes LiPON widely used as a protective interfacial coating on battery electrodes and electrolytes, where it provides chemical inertness and interfacial stabilization.[80]

Oxyhalide glass. Several oxyhalide amorphous solid electrolytes, referred to as AMCO (where A = Li/Na; M = Mg, Al, Zr, Ta, Nb, *etc*; C = Cl, I), have been developed in recent years,[64,66,81–86] and exhibit both high ionic conductivity and good electrochemical stability. Among these oxyhalide GSEs, systems based on earth-abundant metals such as aluminum (LiAlClO[86]) and zirconum (LiZrClO[64,82]) are particularly promising. These compositions offer a cost-effective alternative to high-ionic conductivity halides (*e.g.* Li_3YCl_6, Li_3InCl_6), which often contain expensive rare elements. This strategy is illustrated by the work of Dai *et al.*, who demonstrated that partial oxygen incorporation can transform the low-conductivity crystalline $LiAlCl_4$ into a vitreous lithium–aluminum oxychloride glass with significantly enhanced ionic conductivity.[86] You *et al.* proposed a trimer-like $Si_3O_2Cl_8$ structural motif for such this glass; their experimental indicate that the resulting GSE lacks ionic O–Li bonding, and that Cl^- anions undergo rotational motion.[85] The introducing of oxygen promote glass formation without forming non-bridging oxygen species, thereby increasing free volume and enable greater Cl^- rotational dynamics, which in turn facilitate Li^+ diffusion.[87]

3. Machine learning force fields

The previous section discussed the breadth of SSEs chemistries and their rapid progress. Computational methods, particularly molecular dynamics (MD) simulations, are well suited to bridge the gap between macroscopic transport properties and atomic-level structural features, providing multiscale insights to guide materials optimization.

Historically, computational studies of SSEs have relied primarily on density functional theory (DFT). While DFT is highly accurate, its computational cost restricts accessible length and time scales. This is a critical limitation because cation diffusion and anion dynamics in SSEs are slow processes that require long simulations, and because mesoscale features—such as interfaces with cathodes or Li metal anodes and grain boundaries within the electrolyte—can strongly influence performance. The classical force fields, which use fixed functional forms and empirical parameters, often lack the flexibility and accuracy needed across diverse SSE chemistries.[88] Consequently, ML-FFs that approach DFT accuracy while retaining near-classical efficiency are particularly well suited for SSE research, enabling larger systems, longer timescales, and explicit treatment of microstructure.

Development of ML-FFs was pioneered by Behler and Parrinello, who firstly used neural networks to represent potential-energy surfaces (PES).[89] In their high-dimensional neural network potential (HDNNP), the total energy E of a system is decomposed into a sum of atomic contributions.

$$E = \sum E_i$$

Each atomic energy E_i depend on the local chemical environment of atom i. To ensure translational, rotational, and permutational invariance, atomic environments are encoded as atom-centered symmetry functions (descriptors) constructed from the atomic coordinates; these descriptors are then passed to element-specific neural networks to predict E_i.

Most ML-FFs adopt this PES-decomposition framework, obtaining forces as the negative gradient of the learned with respect to atomic positions; by contrast, approaches like symmetric gradient domain machine learning (sGDML) model learn forces directly.[90] The locality assumption—that each atomic contribution depends primarily on its local environment—confers strong transferability across system sizes: models can be trained on small DFT datasets and then applied to large-scale MD simulations. However, it also requires extensive sampling of diverse local environments and can neglect long-range interactions that are important in some systems.[18]

Based on how the atomic energy E_i is mapped from the local environment, ML-FFs can be categorized into kernel-based, linear, and neural network-based models (Fig. 3(a)). Kernel methods represent learning as Gaussian-process or kernel-ridge regression over a similarity measure between local environments; descriptors such as smooth overlap of atomic positions (SOAP) provide rotationally invariant features. Representative models include Gassian approximation potential (GAP)[91] and self-learning and adaptive database (SLAD),[92] and on-the-fly training/inference is available in electronic-structure packages such as Vienna *ab initio* Simulation Package (VASP).[93,94] Linear models, such as moment tensor potential (MTP), express the atomic energy E_i as a linear combination of basis functions, offering computational efficiency and interpretability.[95] Neural network-based models employs deep learning architectures to map local atomic energy to E_i, enabling capture of highly non-linear PES landscapes.[17,96,97] Widely used examples include the original HDNNP[89] (with implementation in aenet,[98] n2p2,[99] Amp,[100] SIMPLE-NN[101]), end-to-end models such as Deep Potential models[96,97,102–104] and NEP,[105,106] and graph neural network-based models such as MACE,[107] NequIP,[108] DPA-3[109] and CHGNet.[110] In next section, we will discuss the commonly used ML-FF models in recent literature on SSEs studies.

3.1 Commonly used ML-FF models in SSE studies

Gaussian approximation potential (GAP). The GAP employs Gaussian process regression with carefully designed local

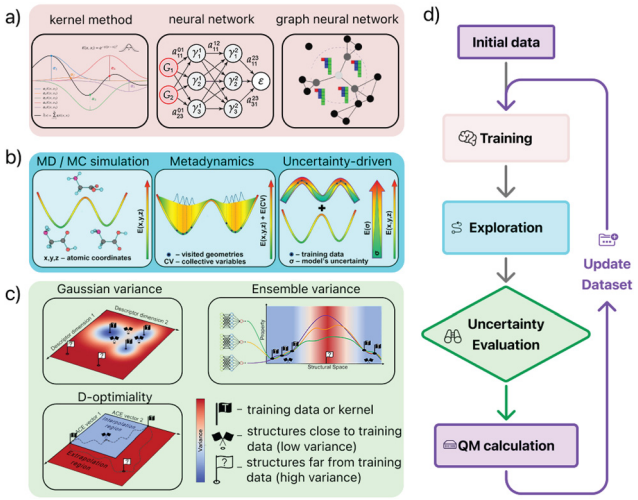

Fig. 3 Machine-learning force fields (ML-FF) and active learning. (a) Schematics of ML-FF architectures—kernel-based, neural-network, and graph neural-network models. (b) Common active-learning sampling strategies. (c) Typical uncertainty-quantification metrics. (d) A generic active-learning workflow. Kernel method illustration adapted from ref. 17. Fig. 6(B) under the terms of CC-BY-NC-ND 4.0 (https://creativecommons.org/licenses/by-nc-nd/4.0/) from American Chemical Society, copyright 2021; neural network schematic adapted from ref. 111. Fig. 1(d) with permission from Wiley, copyright 2019; illustration of graph neural network adapted from ref. 108. Fig. 1(a) under terms of CC-BY 4.0 (https://creativecommons.org/licenses/by/4.0/) from Springer Nature, copyright 2023. Panels b and c adapted from ref. 88. Fig. 7 and 3 under the terms of CC-BY-NC-ND 4.0 (https://creativecommons.org/licenses/by-nc-nd/4.0/) from American Chemical Society, copyright 2024.

kernels.[17,91] In GAP, the atomic energy for a new configuration x_i is predicted as

$$E_i(x_i) = \sum_n K(\mathbf{d}_i, \mathbf{d}_n)$$

where K is the kernel, $\mathbf{d}$ is descriptor, and n are the learned weights. The kernel measures the similarity (covariance) between the test descriptor $\mathbf{d}_i$ and the n-th reference descriptor $\mathbf{d}_n$.

The SOAP descriptor[112] is commonly used in GAP to represent the many-body term,[113] capturing rich geometric detail while remaining smooth and differentiable. As a kernel-based ML-FF, GAP often performs strongly on small to moderate datasets relative to neural-network models.[16,17,92] Its native uncertainty estimates also enable active-learning workflows without ensemble models. However, the inference cost scales with the number of reference environments, which can limit applications to very large or highly complex systems.[17]

Moment rensor potential (MTP). Unlike GAP, which uses Gaussian-process kernels, the MTP represents the atomic energy E_i as a linear expansion in a systematically improvable basis constructed from moment tensors of the neighboring environment:

$$E_i = \sum \xi_\alpha B_\alpha(\mathbf{n}_i)$$

where ξ_α are trainable parameters and B_α are the basis functions. The basis functions B_α are invariant polynomials constructed from contractions of moment tensor descriptors. Similar to GAP, MTP often achieves faster training convergence from scratch than neural-network-based approaches, while retaining good accuracy and transferability.[114]

Drautz later introduced the atomic cluster expansion (ACE), which expresses atomic properties (such as atom's energy) as a systematic body-order expansion using basis functions constructed from radial functions and spherical harmonics.[115] This means that contributions from one-body, two-body, three-body, and higher-order interactions are all included through a complete set of radial and angular basis functions representing the local environment. As a result, ACE offers a complete and efficient general framework for representing atomic interactions.[116] Drautz also demonstrated that many existing interatomic potentials can be viewed as special cases of the ACE formalism,[115] including the previous mentioned ML-FFs such as the MTP, SOAP-GAP, SNAP.[95,112,117] This aspect reveals ACE's broad applicability and significance in the development of ML-FFs.

Deep potential model. Handcrafted descriptors often do not generalize well across various chemical systems and typically require human intervention for specific settings and optimization.[17,97] To overcome these limitations of descriptor-based neural-network ML-FFs, Zhang *et al.* introduced the deep potential (DP) model as an end-to-end approach.[97]

In DP, the atomic energy E_i is obtained *via* two coupled networks: an embedding (encoding) network that maps the local atomic environment into a symmetry-preserving feature space (respecting translational, rotational, and permutational invariance), and a fitting network that converts these features into E_i. By learning the representation directly from data, DP obviates the need for hand-crafted descriptors. DP has been widely applied in SSEs studies, delivering an excellent balance between near-DFT accuracy and computational efficiency.

Neural equivariant interatomic potential (NequIP). The NequIP is an ML-FF model belong to the class of E(3)-equivariant graph neural network (GNN).[118,119] In GNN-based ML-FFs, a molecular or condensed-matter systems is represented as undirected graphs whose nodes are atoms and whose edges connect neighbors within a cutoff. The atomic energy E_i is obtained from the sequence of node embedding *via* trainable readout functions, such as,

$$E_i = \sum R_t\left(\sigma_i^{(t)}\right)$$

where $\sigma_i^{(t)}$ is state of each node i in layer t, R_t is the trainable readout function. In some GNN-based ML-FF architecture, an additional energy bias or scaling term $e(Z_i)$ will be introduced for each atom type.[109] Through message-passing operations, information flows along edges so the model can encode interatomic interactions.

Earlier neural network typically enforced symmetry using invariant scalar features. NequIP instead employs tensor (irreducible) features that transform equivariantly under 3D rotations and reflections, ensuring that predicted energies and

forces obey $E(3)$ symmetry by construction. GNN-based ML-FFs such as NequIP can achieve data efficiency comparable to kernel methods while retaining neural networks' flexibility.[108]

GNN-based ML-FFs are considered semi-local because their layered message-passing architecture enables the capture of interactions beyond the typical cutoff distance. These models are, however, often more computationally intensive than descriptor-based or simple NN potentials due to (1) substantial communication and memory traffic from multi-hop message passing over large atomic neighborhoods,[120,121] and (2) the expensive Clebsch–Gordan tensor products required for equivariant feature coupling. Efforts to reduce this overhead include GPU-optimized implementations[122] and architectural innovations such as Allegro's strictly local message-passing scheme, which reduce the number of interactions and improves parallel scalability,[121] albeit at the cost of neglecting long-range interactions. Alternatively, ML-FFs such as the cartesian atomic cluster expansion[123] (CACE) and the cartesian atomic moment potential[124] (CAMP) construct invariant features directly in the Cartesian space, eliminating the need for spherical harmonics. This Cartesian approach avoids the computationally intensive Clebsch–Gordan tensor operations, offers greater simplicity, and improved computation efficiency.[124]

3.2 Active learning in ML-FFs

ML-FFs are generally unreliable under extrapolation and provide trustworthy predictions only within the domain spanned by their training data.[17] As many SSE-focused ML-FFs now achieve high accuracy (*e.g.* energy errors <10 meV per atom), as shown in Table 1, performance depends increasingly on the breadth and fidelity of the training set rather than on architectural choice. Consequently, ML-FF development demands

Table 1 List of studies of machine learning force fields for solid-state electrolytes. AL: active learning; AIMD: *ab initio* molecular dynamics. Numbers in parentheses indicate GNN interaction layers

System		Year	ML-FF model	DFT level of theory	Data generation scheme	Cutoff (Å)	Energy error (meV per atom)	Force Error (eV Å^{-1})	Ref.
Thiophosphate	Li–P–S	2021	MTP	optB88-vdw	AIMD	5	2.07[a]	0.09	132
		2023	MTP	PBE	AIMD	5	3.86[a]	0.12	133
		2024	GAP	PBE0, PBEsol, r2SCAN	AIMD	5	7.0[b]	0.17	134
		2024	HDNNP	PBE	AIMD	7	12.7[b]	0.24	135
		2024	aenet	PBE	AIMD		3[b]		136
	Li–Si–P–S	2024	DeepMD	PBEsol	AL	6	7.57[b]	0.12	137
	Li–P–S–B–O	2023	MTP	PBE	AL		4.43[a]	0.14	138
	Na–P–S	2023	NNP pre-trained model				3.12[b]		139
		2021	DeepMD	PBE	AIMD				140
		2025	MACE	PBE + D3	AIMD	6(× 2)	14[a]	0.03	141
	Na–P–S–O	2024	DeepMD	PBE + D3	AIMD	6	9.74[b]	0.21	142
	Na–P–S–W	2024	Allegro	r2SCAN	AIMD	6.5(× 2)	0.38[b]	0.03	143
LGPS-type	Li–Ge–P–S	2023	PaiNN	PBE	AL	5(× 3)	13.74[a]	0.03	144
		2023	MTP	PBE	AIMD	5	2.5[a]	0.07	133
	Li–{Ge,Si,Sn}–P–S	2021	DeepMD	PBEsol,PBE	AL	6	1.33[b]	0.08	145
LLZO-system	Li–La–Zr–O	2022	NNP	PBE	AIMD	6	3.7[b]	0.17	146
		2024	NEP	PBEsol	AL	7.5	0.66[b]	0.06	147
		2024	DeepMD	PBE	Metadynamics	6	8.51[b]	0.27	148
	Li–La–Zr–O–Nb	2018	SALD	WC	AIMD	5.2917	11.7[a]	0.26	149
Perovskite-type	Li–La–Ti–O	2021	MTP	optB88-vdw	AIMD	5			132
	Li–Sr–Ta–Hf–O	2025	DeepMD	PBE	AIMD	6			150
NASICON	Li–Ge–P–O	2024	DeepMD	PBE	AL	7	5.79[b]	0.26	151
KTP-type	Na–Ga–P–O–F	2025	MTP	PBE	AL		1[b]	0.14	152
Argyrodite	Li–P–S–Cl	2024	MTP	PBE	AL	5	6.9	0.16	61
		2024	MTP	PBE	AL	5	17.8[b]		153
		2025	DeepMD	PBE	AL	8	1.34[b]	0.05	63
		2025	MTP	PBE + D3	AL	5			154
		2025	MTP	optB88-vdw	AIMD		7.5[b]	0.37	25
	Li–P–S–{Cl,Br,I}	2024	MTP	optB88-vdw	AL	5	3[a]	0.1	155
	Li–P–S–Cl–O–C	2025	NequIP	PBE	AIMD	8(× 4)	0.5[a]	0.01	156
Halide	Li–Y–Cl	2021	MTP	optB88-vdw	AIMD		1.11[b]	0.04	132
	Li–Y–Br	2023	MTP	PBE	AIMD	5	1.05[a]	0.05	133
	Li–Er–Cl	2023	MTP	PBE	AIMD	5	2.57[a]	0.05	133
	Na–{Nb,Ta}–Cl	2025	DeepMD	PBE	AIMD	8	1.6[a]	0.03	157
	Li–Nb–Ta–Cl	2024	GAP	PBE	AIMD			0.075	158
Closo-hydroborate	Li–B–H	2017	SLAD	PBE	AIMD	4.23	2.6[a]	0.15	92
		2023	MTP	rev-vdW-DF2,PBE,PBE-D3	AL		1[b]	0.08	159
		2025	DeepMD	PBE	AL	6	0.59[a]	0.01	160
	Na–C–B–H	2025	DeepMD	rev-vdW-DF2	AL	7	1.26[b]	0.04	161
Li–N		2019	eSNAP	PBE	AL		0.9[a]	3.77	162
		2023	GAP	PBEsol	AIMD	5	3.61[b]	0.04	163
Li–P		2023	MTP	PBE	AL		18.5[b]	0.34	164
LIPON		2025	NequIP	PBE	AIMD	4.3(× 6)	5.5[a]	0.01	165

[a] Mean absolute error (MAE). [b] Root mean squared error (RMSE).

datasets with both comprehensive configurational coverage and high-quality labels to ensure reliability across the relevant configuration space.

Training data may be drawn from existing DFT datasets—most commonly *ab initio* molecular dynamics (AIMD)—or generated *via* active-learning workflows (Fig. 3(b)). AIMD is computationally expensive and can under sample rare but mechanistically important high-energy events because Boltzmann statistics overrepresent low-energy regions. Moreover, AIMD is often performed at reduced precision (*e.g.*, coarser *k*-point meshes and lower plane-wave cutoffs) relative to single-point calculations, which can degrade label quality.[125] Active learning offers a systematic alternative: a provisional ML-FF explores configuration space, while uncertainty or diversity criteria select configurations for DFT labeling, preserving efficiency while expanding coverage.[126]

The general active learning workflow comprises four iterative stages, as shown in Fig. 3(b): training, exploring, uncertainty evaluation, and labelling.[127,128] Starting with an initial model (or ensemble) trained on an initial dataset, MD simulations use the current ML-FF to explore configuration space. When configurations exceed a predefined uncertainty threshold, they are selected for DFT calculations. The newly labelled data are then added to the training set, and the model is retrained. This approach has been formalized in automated pipelines such as DP-GEN,[128] which systematizes the DP active learning loop with minimum human intervene.

Two exploration strategies are commonly used (Fig. 3(c)): (1) conventional MD simulations or Monte Carlo (MC) sampling, typically in NPT or NVT ensembles, to sample thermodynamically accessible configurations; and (2) the metadynamics sampling, which applies bias potentials along carefully chosen collective variables (CVs) to access rare events and high-energy regions. Metadynamics offers superior exploration of rare events but requires system-specific CV selection and tuning. A recent alternative is uncertainty-driven sampling, which uses model uncertainty as a bias to steer exploration toward regions where the ML-FF is least reliable.[129]

Common uncertainty metrics (Fig. 3(d)) include: (a) Gaussian Gaussian-process predictive variance, available natively in GAP-type ML-FFs; (b) D-optimality criteria, used in MTP *via* an extrapolation grade derived from the determinant of the information matrix; and (c) ensemble disagreement, in which multiple models with different random initializations are trained and the dispersion in predicted forces is used as the uncertainty estimate.[93,127,130] Ensemble methods are model-agnostic and generally robust, and are therefore widely adopted across ML-FF frameworks.[131]

4. The application of ML-FFs in SSEs research

4.1 Identification of GSEs

Because of their amorphous character, glassy SSEs present unique structural challenges that require specialized approaches for accurate atomic modeling. As shown in Fig. 4, the atomic structures can be generated either by reverse Monte Carlo (RMC) fitting to experimental data[166,167] or by melt-quenching simulations.[16,168,169]

The RMC method employs the Metropolis acceptance–rejection algorithm to minimize the difference between simulated and experimental features (Fig. 4(a)). However, in its basic form RMC is under-constrained and can yield chemically unreasonable networks, particularly in systems with complex bonding. A hybrid RMC-MLFF approach (RMC-DL) has been proposed to address this issue,[171] using an ML-FF to assess the energetic plausibility and thereby produce more physically meaningful structures, as demonstrated by Yamada *et al.*[136]

An alternative is to use ML-FFs directly to perform melt-quench simulations (Fig. 4(b)). Due to their scalability, ML-FFs enable larger supercells and longer trajectories than AIMD while retaining near-DFT accuracy, yielding more representative amorphous networks. This strategy has been applied across multiple glassy SSE families, including halide glass,[158,172] sulfide glass,[135,137,141,142] LiPON glass,[165] amorphous LLZO systems,[148] and metal oxyhalide systems.[85–87]

However, developing ML-FFs for amorphous systems is hampered by limited training data: metastable amorphous phases are largely absent from open datasets and, by extension, from pre-trained models. Recent evaluations of available pre-trained ML-FFs have identified unphysical structural motifs and poor agreement with measured mechanical properties.

We recently developed ML-FF models for Li-thiophosphate GSE and Na-oxythiophosphate GSEs (Fig. 5), namely, Li_2S–SiS_2–P_2S_5 and $Na_3PS_{4-x}O_x$ systems.[137,142] These ML-FFs reproduce experimental densities, structure factors, radial distribution

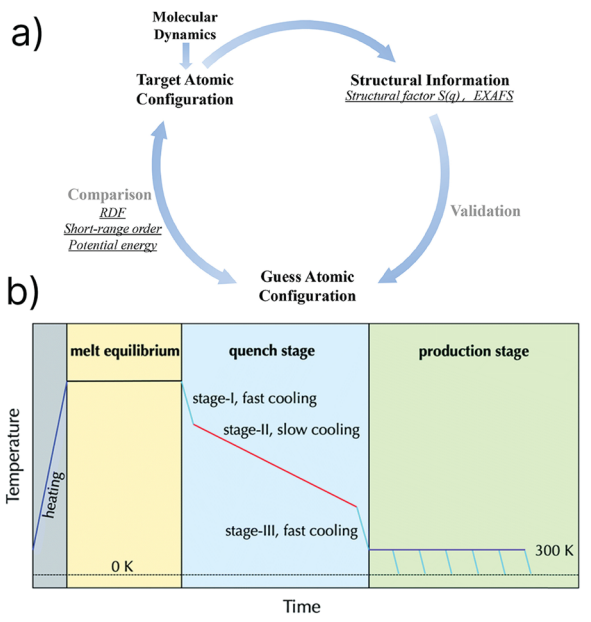

Fig. 4 Workflow of obtaining glass structures. (a) reverse Monte Carlo (RMC) method. (b) Melt-Quenching simulation. Panel (a) reprint from ref. 170 with permission from Wiley, copyright 2023; panel (b) reprint from ref. 168 with permission from The Royal Society of Chemistry, copyright 2022.

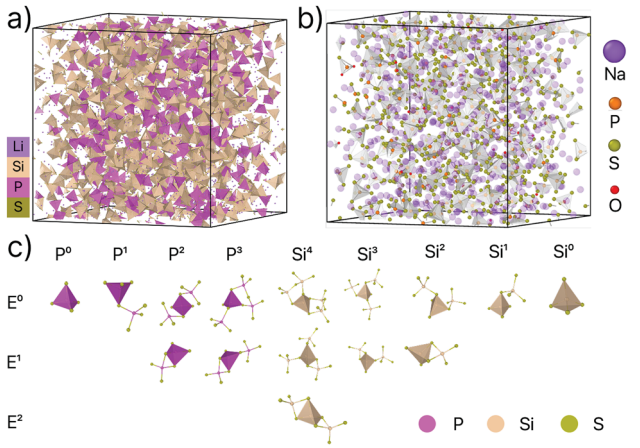

Fig. 5 Structure of obtained $Li_2S–SiS_2–P_2S_5$ and $Na_3PS_{4-x}O_x$ glass through ML-FF melt-quenching simulations. (a) $60Li_2S–2SiS_2–8P_2S_5$ (b) $Na_3PS_{3.85}O_{0.15}$. (c) local environments of P and Si. Pictures adapted form ref. 142 with permission from American Chemical Society, copyright 2023 and ref. 137 with permission from The Royal Society of Chemistry, copyright 2024.

functions, and mechanical properties. The larger simulation cells accessible with ML-FF-driven melt-quench workflows enable robust statistics; by contrast, typical AIMD supercells (~100 atoms) provide insufficient sampling for reliable structural analysis.

Using these ML-FFs, we examined (1) oxygen doping in NaPSO ($Na_3PS_{4-x}O_x$) and (2) incorporation of a second network former in Li-thiophosphate glasses. In the $Li_2S–SiS_2–P_2S_5$ system, compositional scans reveal that the medium-range connectivity of short-range structural units (edge sharing, corner sharing, or isolated motifs shown in Fig. 5(a) and (c)) strongly modulates Li-ion diffusion. In $Na_3PS_4{-}_xO_x$, oxygen exerts dual effects—reducing free volume *via* increased electronegativity while simultaneously enhancing network flexibility—together governing ionic transport.

4.2 Phase transition

As discussed in previous sections, many SSEs exhibit temperature-driven polymorphism, with a low-temperature phase (typically low ionic conductivity) and a high-temperature phase (typically higher conductivity). For example, LLZO adopts a high-conductivity cubic phase ($Ia\bar{3}d$) and a low-conductivity tetragonal phase ($I41/acd$), with a phase transition temperature around 900 K that alter Li^+ transport by orders of magnitude. Complex hydrides, commonly transform from ordered monoclinic structures at low temperature to disordered phases at high temperature; in $Na_2B_{10}H_{10}$, the $B_{10}H_{10}^{2-}$ anions undergo an order–disorder transition around ~373 K, enabling superionic conduction.[173] Sulfide electrolytes (*e.g.*, Na_3PS_4) and halide electrolytes (*e.g.*, Li_3YCl_6) likewise display temperature-dependent phase transitions that strongly affect transport properties.

Elucidating the atomistic mechanisms of these transitions is crucial for devising strategies to stabilize high-conductivity phases at room temperature. By delivering near-DFT accuracy at (near) classical MD cost, ML-FFs enable the long trajectories and large cells needed to capture nucleation pathways and order–disorder dynamics—capabilities beyond classical force fields and typically inaccessible to AIMD. As shown in Fig. 6(a)–(g), Shimizu *et al.* tracked the crystallization of Li_3PS_4 glass over ~100 ns, a timescale infeasible for AIMD. Maltsev *et al.* investigate the temperature-induces order–disorder phase transition in $Li_2B_{12}H_{12}$ (Fig. 6(h) and (i)) and $LiCB_{11}H_{12}$ and compared the effects of different exchange–correlation functionals on crystal structure and phase transition temperature.

We developed ML-FFs for the Na–C–B–H *closo*-hydroborate family and investigated the temperature-induced transition in $Na_2B_{12}H_{12}$, as shown in Fig. 6(j) and (k) The simulations reveal a martensitic, Bain-like pathway from the room-temperature monoclinic phase to a high-temperature bcc phase, accompanied by a pronounced increase in Na^+ conductivity and a reduced barrier for anion reorientation. Despite the smaller unit-cell volume of the bcc phase, the dense network of tetrahedral interstitials, together with faster anion reorientation, yields abundant, dynamically connected migration pathways that enable rapid Na^+ diffusion.

4.3 Room temperature calculation

A primary goal of computation is to quantify ionic conductivity and migration barriers at operating temperatures; reliable estimates are essential for SSE screening and optimization. Although AIMD is intrinsically accurate, it faces three major limitations: (1) short trajectories that yield large statistical uncertainties, (2) non-Arrhenius transport in many SSEs that invalidates high-temperature extrapolation, and (3) computational cost that restricts accessible length and time scales.

Statistical errors arise because AIMD runs typically span only hundreds of picoseconds, providing too few diffusion events for well-converged transport coefficients. He *et al.* showed that uncertainties in AIMD-derived transport properties can be substantial, especially for the slow diffusion characteristic of room-temperature SSEs.[177] Moreover, as shown in Fig. 7 and 8, the common practice of extrapolating high-T data to room temperature with an Arrhenius law is often unjustified: materials such as LGPS and Li_3YCl_6 exhibit non-Arrhenius behavior due to phase transitions, temperature-dependent diffusion mechanisms, or anion dynamics (*e.g.*, PS_4 rotational modes). In such cases, direct room-temperature calculations are preferable, as Arrhenius extrapolation can lead to errors of orders of magnitude.

4.4 Anion rotational movement

Anions play a crucial role in SSEs performance, serving both as the structural framework and as active participants in cation diffusion. In particular, the rotational dynamics of complex anions (Fig. 9) have emerged as key to understanding superionic conduction.[133,136,157,178–185]

We recently utilized ML-FFs to study anion dynamics in $Li_2S–SiS_2–P_2S_5$ GSE and in $Na_2B_{12}H_{12}$ SSE. For melt-quench glass models of $xLi_2S–(1-x)P_2S_5$ (x = 67%, 70%, 75%), we

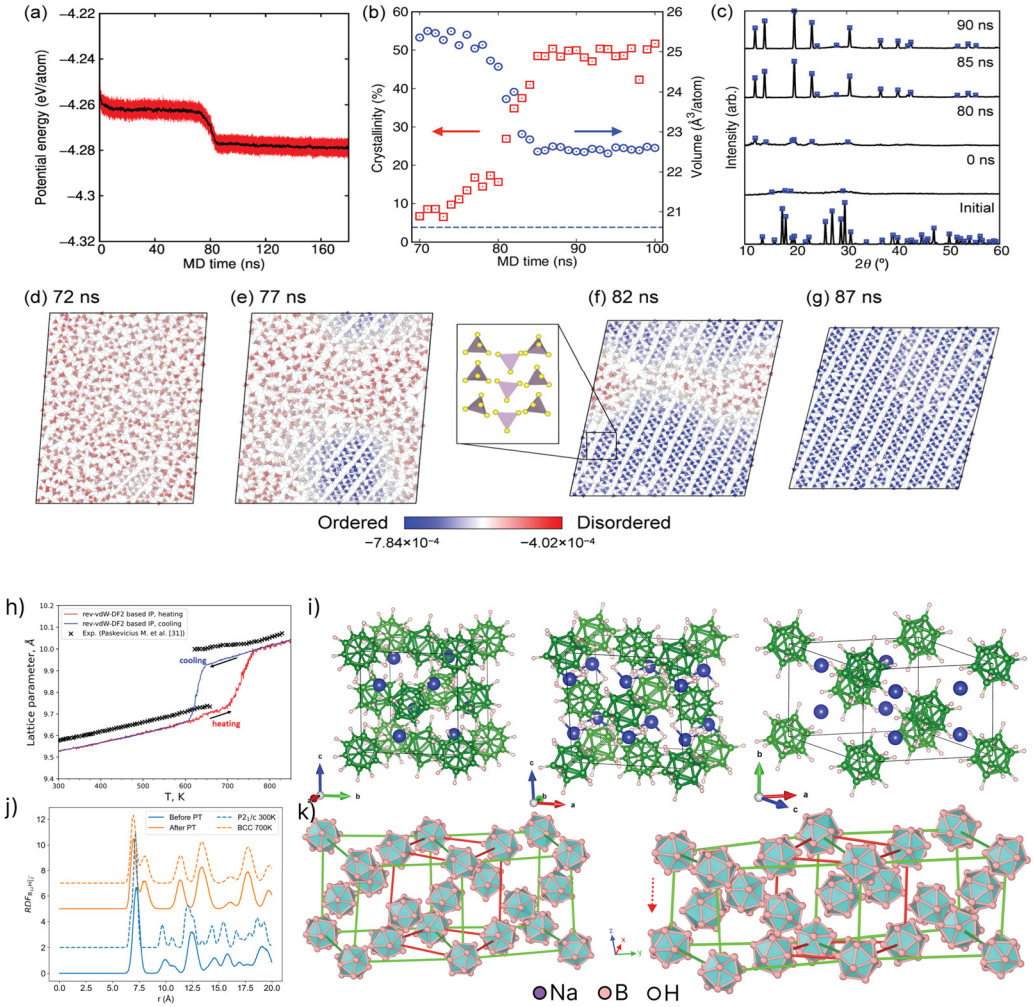

Fig. 6 Phase transition studies in SSEs. (a)–(g) Crystallization process of Li_3PS_4 GSE: (a) potential energy profile, (b) changes in crystallinity and cell volume, (c) calculated XRD pattern, (d)–(g) snapshots from 72 ns to 87 ns. (h), (i) Order–disorder transition of $Li_2B_{12}H_{12}$: (h) lattice constant during heating and cooling, (i) crystal structures of $Li_2B_{12}H_{12}$ cubic and monoclinic phases. (j)–(k) Phase transition in $Na_2B_{12}H_{12}$: (j) pair distribution function of $Na_2B_{12}H_{12}$ before and after phase transition, (k) illustration of Bain martensitic transition path in $Na_2B_{12}H_{12}$. panel a–g reprint from ref. 135 with permission form American Chemical Society, copyright 2024; panel h, i reprint from ref. 174 with permission form American Chemical Society, copyright 2023; panel j, k reprint from ref. 161 with permission form American Chemical Society, copyright 2025.

found that decreasing fractions of corner- and edge-sharing PS units, coupled with increasing isolated PS_4 tetrahedra, lead to more bridging sulfur atoms, which allows for more rotational movement. In $60Li_2S$–$32SiS_2$–$8P_2S_5$ GSE (Fig. 9(c)), calculations of Li^+ diffusion and anion rotation show small-angle rotations ($<20^\circ$) of PS units along the Li^+ diffusion pathways, suggesting that enhanced anion rotational degrees of freedom can lower Li^+ migration barriers.

We applied a similar analysis to $Na_2B_{12}H_{12}$. As shown in Fig. 9(d), in the low-temperature monoclinic phase, $B_{12}H_{12}^{2-}$ anions undergo slow, discrete rotations about symmetry axes (predominantly fivefold), whereas in the high-temperature bcc phase they reorient more rapidly with frequent hops between symmetry-equivalent orientations. Fitting the orientational autocorrelation to an exponential yields Arrhenius behavior (Fig. 9(e)): the reorientation rate increases by $\sim 20\times$ in the high-T phase, and the activation energy drops from 0.77 eV to 0.18 eV.

The paddle-wheel effect has been a subject of considerable debate in the SSEs community.[157,160,178,179] This debate stems partly from the lack of a unified definition.[178] Regardless, it is well agreed that rotational motion of anions can lower cation migration energy barriers, as illustrated in Fig. 9(a). AIMD simulations by Smith and Siegel (Fig. 9(b)) suggest that such effects can operate at room temperature in glassy electrolytes: in Li_3PS_4 glass, PS_4^{3-} tetrahedra exhibit large rotational displacements ($\sim$20–75°) that are temporally and spatially correlated with Li^+ migration events.[179]

However, recent ML-FF studies have deepened our understanding of anion rotation effects. Xu *et al.* employed MTP to investigate polyanion rotation effects across multiple SSEs systems (β-Li_3PS_4, $Li_7P_3S_{11}$, $Li_{10}GeP_2S_{12}$, Li_3ErCl_6, Li_3YBr_6)

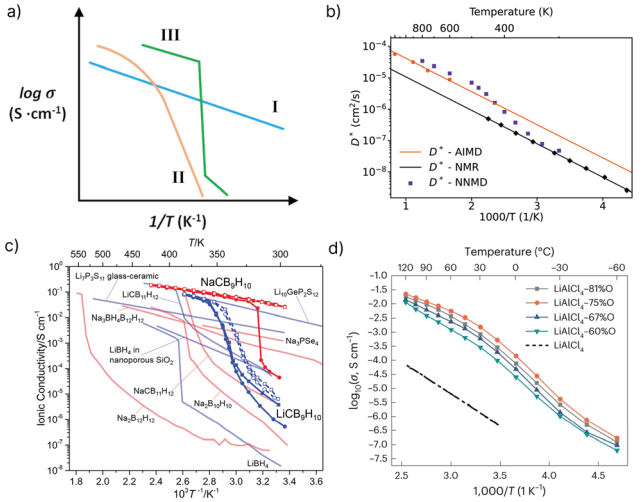

Fig. 7 Temperature-dependent ionic conductivity. (a) Schematic illustration of three types of conductivity-temperature relationships, (b)–(d) Arrhenius ionic conductivity of LGPS, *closo*-hydroborate SSEs, glassy LiAlClO SSEs. Panel (a) reprinted from ref. 145 with the permission of AIP Publishing, copyright 2021; panel (b) reprinted from ref. 144 (Winter *et al.*, 2023) under terms of CC-BY 4.0 (https://creativecommons.org/licenses/by/4.0/) from IOP Publishing, copyright 2023; panel (c) reprinted from ref. 175 with permission from Wiley, copyright 2016; panel (d) reprinted from ref. 86 with permission from Springer Nature, copyright 2023.

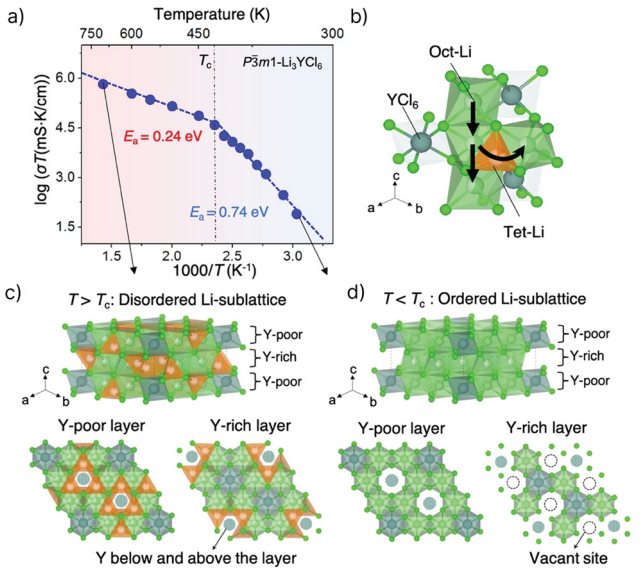

Fig. 8 Super-ionic transition in Li_3YCl_6. (a) Arrhenius plot of Li+ conductivity, (b) Li^+ migration pathways in Li_3YCl_6, (c) structure of partially occupied Li^+ sites in Li_3YCl_6, (d) structure of ordered Li^+ sublattice in Li_3YCl_6. Reprinted from ref. 176 under the terms of CC-BY-NC-ND 4.0 (https://creativecommons.org/licenses/by-nc-nd/4.0/) from Wiley, copyright 2023.

using μs-scale simulations.[133] Surprisingly, they found that only $Li_7P_3S_{11}$ shows significant polyanion rotation at room temperature, and that rotational $[PS_4]^{3-}$ groups correlate weakly and negatively with Li^+ diffusion, challenging the notion of pervasive paddle-wheel–assisted transport in crystalline systems at ambient conditions.

The current understanding suggests that the paddle-wheel effect requires careful consideration of several factors: (1) the need for a strict definition based on quantitative metrics rather than qualitative observations,[178] and (2) understanding that its importance varies significantly between different materials and temperature regimes. ML-FF simulations provide the temporal and spatial resolution needed to disentangle coupled cation–anion dynamics and to assess these effects rigorously.

4.5 Interface study

ML-FFs are particularly well suited to interface studies for three reasons: (1) they enable simulations of large interfacial regions with adequate statistical sampling; (2) they access the extended time scales required to capture slow interfacial processes; and (3) they explicitly describe bond breaking and formation, allowing direct treatment of interfacial chemistry. These capabilities make ML-FFs especially valuable for elucidating grain-boundary transport, surface reactions, and solid–solid interfaces in SSEs.

Grain boundary. Grain-boundaries (GBs) effects vary across SSEs systems. In oxide-based SSEs, GBs typically impede Li^+ transport and potentially promote dendrite growth, whereas in systems such as Li_3InCl_6 and Li_3PS_4 they often enhance Li diffusion due to local amorphization. ML-FF enables detailed, atomic-scale investigation of GBs structures and transport properties that would be prohibitively expensive with AIMD. As shown in Fig. 10, Ou *et al.* modeled Σ3 and Σ5 GBs in argyrodite Li_6PS_5Cl[61] and showed that the opening of Li-coordinated cages at GBs strongly influences Li^+ diffusion (Fig. 10(b)). You *et al.* recently utilized an ML-FF to study the vertical and horizontal GBs in LLZO garnet-type SSEs; in that case, GB amorphization hinders Li transport but suppresses Li aggregation and inhibits dendrite formation.[186]

Collectively, recent computational[61,186] and experimental[187] studies have demonstrated that grain boundary engineering can be employed to optimize the performance of SSE by enhancing ionic conductivity and suppressing dendrite formation. Specific strategies include inducing amorphization and increasing vacancy concentrations at GBs.[138,187] By elucidating the atomic-level structure–transport relationships at interfaces, researchers can design targeted synthesis and post-processing approaches to minimize GB resistance. This progress presents both opportunities and challenges for ML-FF modelling. One on hand, ML-FFs enable simulations involving thousands of atoms with near-DFT accuracy. On the other hand, complex atomic environments, composed of metastable amorphous and defect-rich phases, pose significant challenges for data-driven ML-FF approaches. Addressing these challenges requires the development of ML-FF models with exceptional generalizability, supported by comprehensive datasets that capture the full spectrum of structural diversity.

SSE-surface reactions. Surface stability is crucial for SSEs processing and long-term performance. Li *et al.* used an ML-FF to study gas–solid reaction dynamics on Li_6PS_5Cl surfaces

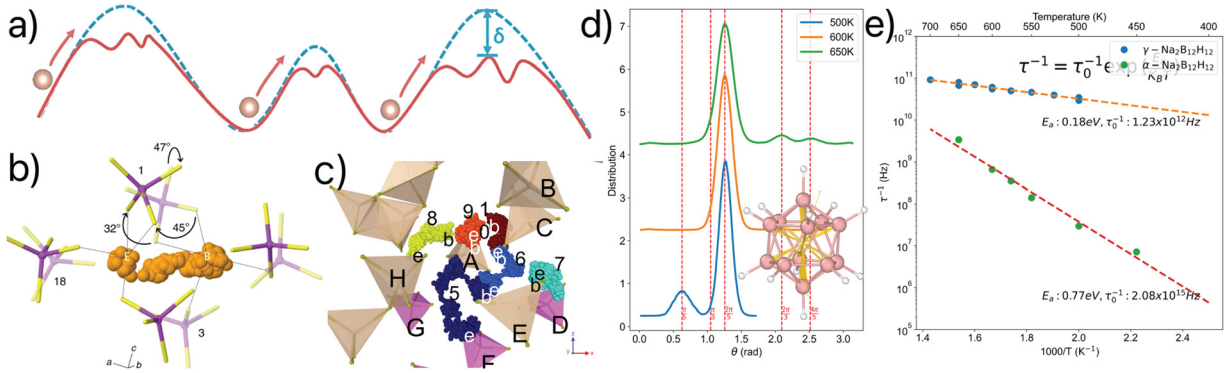

Fig. 9 Anion rotation in SSEs. (a) Illustration of the effect of anion rotation on lowering cation migration energy barrier, (b) illustration of the coupling of cation transport with the reorientation of anions in LPS glass, (c) Li^+ diffusion trajectories in $60Li_2S–32SiS_2–8P_2S_5$ glass over 30 ps, with PS_4 (purple) and SiS_4 (brown) tetrahedra, (d) anion rotation angle and axis in low-temperature $Na_2B_{12}H_{12}$ phases, (e) Arrhenius plot of anion reorientational speed in high-temperature (γ) phase and low-temperature (α) $Na_2B_{12}H_{12}$ phase. Panel (a) adapted from abstract image of ref. 180 with permission from Elsevier, copyright 2024; panel (b) reprinted from ref. 179 (Smith *et al.*, 2020) under terms of CC-BY 4.0 (**https://creativecommons.org/licenses/by/4.0/**); panel (c) reprinted from ref. 137 with permission form American Chemical Society, copyright 2024; panels (d)–(e) reprinted from ref. 161 with permission form American Chemical Society, copyright 2025.

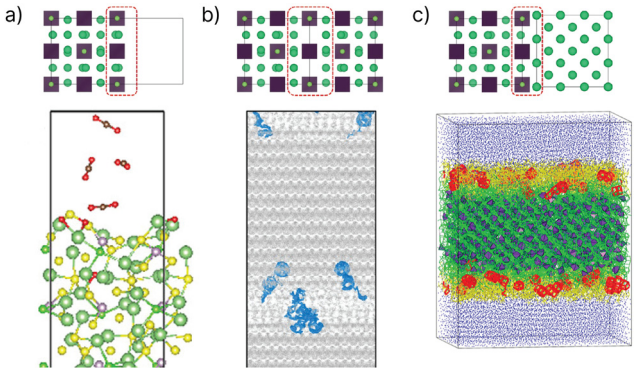

Fig. 10 Solid-state electrolyte interface schematics (top row) and atomic models in argyrodite SSEs (bottom row): (a) surface of argyrodite. (b) Argyrodite Σ5 grain boundary model and Li diffusion trajectory (blue). (c) Argyrodite|Li metal interface after 90 ps. Top row schematics from ref. 13 with permission from Springer Nature, copyright 2025; bottom models adapted from ref. 156 with permission form American Chemical Society, copyright 2025, ref. 61 with permission form American Physical Society, copyright 2024, and ref. 153 with permission form American Chemical Society, copyright 2024, respectively.

under CO_2 and mixed CO_2/O_2 atmospheres (Fig. 10(a)).[156] Their NequIP model enabled nanosecond-scale simulations that revealed detailed reaction mechanisms impossible to AIMD approaches.

The study demonstrated that in pure CO_2, the surface evolves toward Li_2CO_2S *via* C–S bond formation, whereas in CO_2/O_2 mixtures O_2-mediated pathways favor Li_2CO_3. These insights clarify how ambient gases govern surface chemistry during synthesis and operation, informing atmospheric processing conditions and protective-coating strategies. More broadly, the ability to model gas–solid reactions with near-chemical accuracy over extended timescales provides a powerful route to dissect SSE degradation mechanisms.

Metal-SSE interfaces. The solid electrolyte interphase (SEI) is a critical component of ASSBs, yet most studies lack the atomic-level resolution necessary to elucidate reaction pathways and structural evolution. Hence, it is important to study and understand the reaction of SEI in SSEs. Using ML-FF, Ren *et al.* studied the SEI formation at a β-Li_3PS_4/Li-meal contact at 300 K.[188] Their MD simulations reveal a 4 stage process: (1) a brief interdiffusion stage in which interfacial S and P migrate toward the Li metal while Li migrates into the electrolyte, producing an amorphous SEI with a mutual diffusion depth up to ∼41 Å; (2) nucleation of a crystalline interphase at the interface; (3) anisotropic growth that proceeds rapidly parallel to the Li surface with comparatively slow thickening and, once the surface is covered, expansion toward the SSE; and (4) a quasi-steady-state regime in which SEI thickening slows and the structure stabilizes.

Most current ML-FFs cannot capture electrochemical charging/discharging, limiting their ability to model dendrite nucleation or SEI evolution under redox driving forces. To address this gap, Hu *et al.* introduced the DP-QEq framework, which enables constant-charge or constant-potential simulations by decomposing the total energy into a short-range part learned by the ML-FF and a long-range part treated *via* charge equilibration (QEq).[189,190] This approach allows explicit control of electrochemical driving forces at SSE–electrode interfaces, enabling mechanistic studies of SEI formation, growth, and stability.

5. Future perspective and conclusion

Transferability between different studies

Transferability remains a major challenge for ML-FFs, arising from both architectural differences and heterogeneity in training data. Although numerous SSE-focused ML-FFs and large datasets now exist, models trained in one framework are rarely usable without modification in another.

Data are generated at different levels of precision, using different DFT software, exchange–correlation functionals,

Hubbard-U corrections, and van der Waals interactions, complicating cross-study reuse. The explored configurations spaces also differ substantially. For instance, in Table 1, a ternary Li–P–S ML-FF could be trained on crystalline β-Li_3PS_4 alone or with different degrees of disorder,[133] on other Li_3PS_4 polymorphs or related thiophosphates,[134] on decomposition products such as Li_2S and Li_3P,[145] on amorphous/glassy structures,[137] or on Li–metal interfaces.[188] The adoption of active learning in SSEs studies also depends heavily on software ecosystems, with MTP and DP showing greater usage due to their integration with established software packages, such as DP-GEN and MLIP.[120,127,128,191] Moreover, active-learning datasets are themselves conditioned by the underlying ML-FF architecture, further hindering transfer between models.[192]

As a result, new systems often require training from scratch. A pragmatic path forward is a pre-trained ''foundation model'' plus fine-tuning: large models trained on broad datasets learn transferable atomic-environment embeddings, which can then be adapted efficiently to target chemistries with system-specific data, often achieving higher accuracy and computational efficiency.[130,193–196]

From bulk to interfaces

Most ML-FF studies focus on bulk SSE materials, but there is growing need for a deeper understanding of interfaces: SSE–metal anode, SSE-high voltage cathode, and SSE–SSE interfaces. To date, relatively few ML-FF studies have examined interfaces; most target SSE–metal and SSE–SSE systems, with only limited studies on SSE–cathode interfaces.

From the ML-FF development perspective, SSE–cathode interfaces are especially challenging because they introduce additional elements and compounds. Many ML-FFs use element-specific descriptors or networks to improve accuracy, so expanding the chemical space increases data requirements and can slow inference. Moreover, transition-metal species such as Ni, Co, and Mn add complexity through variable oxidation states, strong correlation, and spin degrees of freedom.[197,198]

Understanding how interfaces behave under realistic mechanical and electrochemical conditions is critical for advancing solid-state systems. This includes accounting for GPa-level stress[199] buildup at the interfaces and the variations in chemical potentials that occur during electrochemical cycling.[73] Recent advances in ML-FFs are beginning to address these challenges. These developments include models designed to capture long-range interactions (*e.g.*, 4G-HDNNP,[200] DPLR,[201] Latent Ewald Summation[202]) as well as those designed to predict additional scalar and tensor properties, such as charge states (*e.g.*, CHGNET[110]), spin (*e.g.*, DeepSPIN[197]), and dynamic charge-related properties such as the Born effective charge (*e.g.*, Equivar,[203] CACE-LR[204]). While these advanced models enable more accurate and physically informed descriptions of interfacial phenomena, their performance remains fundamentally limited by the quality and diversity of their training data. This reveals the urgent need for active learning workflows and pre-trained models to efficiently sample, explore, and generalize across these highly complex systems.[196]

In conclusion, ML-FFs have emerged as a powerful computational tool for studying solid-state electrolytes, bridging the gap between the first-principles accuracy and the large-scale, long-timescale simulations required to understand these complex materials. As revealed in this review, the application of ML-FFs has already provided critical atomic-level insights across a wide range of crystalline and glassy SSEs, from accurate modeling of structures and mechanical properties to the study of complex transport dynamics and reactions. The growing interest in the interfacial phenomena and studies under more realistic mechanical and electrochemical conditions demands even more accurate ML-FF models and comprehensive, diverse training datasets. Recent advances, including the development of long-range models, foundation models, and active learning workflows, enables promising pathways towards a deeper atomic-level understanding of solid electrolytes, ultimately accelerating the discovery and optimization of robust, high-performance materials for next generation all-solid-state batteries.

Conflicts of interest

There are no conflicts to declare.

Data availability

No primary research results, software or code have been included, and no new data were generated or analysed as part of this review.

Acknowledgements

This work was supported by the start-up grant at Iowa State University.

Notes and references

1 B. Dunn, H. Kamath and J.-M. Tarascon, *Science*, 2011, **334**, 928–935.
2 J. Janek and W. G. Zeier, *Nat. Energy*, 2016, **1**, 16141.
3 X. Zeng, M. Li, D. Abd El-Hady, W. Alshitari, A. S. Al-Bogami, J. Lu and K. Amine, *Adv. Energy Mater.*, 2019, **9**, 1900161.
4 P. Albertus, V. Anandan, C. Ban, N. Balsara, I. Belharouak, J. Buettner-Garrett, Z. Chen, C. Daniel, M. Doeff, N. J. Dudney, B. Dunn, S. J. Harris, S. Herle, E. Herbert, S. Kalnaus, J. A. Libera, D. Lu, S. Martin, B. D. McCloskey, M. T. McDowell, Y. S. Meng, J. Nanda, J. Sakamoto, E. C. Self, S. Tepavcevic, E. Wachsman, C. Wang, A. S. Westover, J. Xiao and T. Yersak, *ACS Energy Lett.*, 2021, 1399–1404.
5 A. C. Ngandjong, T. Lombardo, E. N. Primo, M. Chouchane, A. Shodiev, O. Arcelus and A. A. Franco, *J. Power Sources*, 2021, **485**, 229320.
6 J. C. Garcia, J. Gabriel, N. H. Paulson, J. Low, M. Stan and H. Iddir, *J. Phys. Chem. C*, 2021, **127**, 9745–9749.
7 A. Akrouchi, H. Benzidi, A. Al-Shami, A. El Kenz, A. Benyoussef, A. El Kharbachi and O. Mounkachi, *Phys. Chem. Chem. Phys.*, 2021, **23**, 27014–27023.

8 A. Jain, S. P. Ong, G. Hautier, W. Chen, W. D. Richards, S. Dacek, S. Cholia, D. Gunter, D. Skinner, G. Ceder and K. A. Persson, *APL Mater.*, 2013, **1**, 011002.
9 L. Xia, H. Liu and Y. Pei, *Nanoscale*, 2024, **16**, 15481–15501.
10 Y. Liu, O. C. Esan, Z. Pan and L. An, *Energy and AI*, 2021, **3**, 100049.
11 E. Kim, K. Huang, A. Tomala, S. Matthews, E. Strubell, A. Saunders, A. McCallum and E. Olivetti, *Sci. Data*, 2017, **4**, 170127.
12 A. Vasylenko, J. Gamon, B. B. Duff, V. V. Gusev, L. M. Daniels, M. Zanella, J. F. Shin, P. M. Sharp, A. Morscher, R. Chen, A. R. Neale, L. J. Hardwick, J. B. Claridge, F. Blanc, M. W. Gaultois, M. S. Dyer and M. J. Rosseinsky, *Nat. Commun.*, 2021, **12**, 5561.
13 A. C. C. Dutra, B. A. Goldmann, M. S. Islam and J. A. Dawson, *Nat. Rev. Mater.*, 2025, **10**, 566–583.
14 Z. Zhang, Y. Shao, B. Lotsch, Y.-S. Hu, H. Li, J. Janek, L. F. Nazar, C.-W. Nan, J. Maier, M. Armand and L. Chen, *Energy Environ. Sci.*, 2018, **11**, 1945–1976.
15 A. Madanchi, E. Azek, K. Zongo, L. K. Béland, N. Mousseau and L. Simine, *ACS Phys. Chem. Au*, 2025, **5**, 3–16.
16 S. Urata, M. Bertani and A. Pedone, *J. Am. Ceram. Soc.*, 2024, **107**, 7665–7691.
17 O. T. Unke, S. Chmiela, H. E. Sauceda, M. Gastegger, I. Poltavsky, K. T. Schütt, A. Tkatchenko and K.-R. Müller, *Chem. Rev.*, 2021, **121**, 10142–10186.
18 D. M. Anstine and O. Isayev, *J. Phys. Chem. A*, 2023, **127**, 2417–2431.
19 E. Sebti, H. A. Evans, H. Chen, P. M. Richardson, K. M. White, R. Giovine, K. P. Koirala, Y. Xu, E. Gonzalez-Correa, C. Wang, C. M. Brown, A. K. Cheetham, P. Canepa and R. J. Clément, *J. Am. Chem. Soc.*, 2022, **144**, 5795–5811.
20 Y. Xiao, K. Jun, Y. Wang, L. J. Miara, Q. Tu and G. Ceder, *Adv. Energy Mater.*, 2021, **11**, 2101437.
21 R. Schlem, S. Muy, N. Prinz, A. Banik, Y. Shao-Horn, M. Zobel and W. G. Zeier, *Adv. Energy Mater.*, 2020, **10**, 1903719.
22 P. Zhong, S. Gupta, B. Deng, K. Jun and G. Ceder, *ACS Energy Lett.*, 2024, **9**, 2775–2781.
23 M. J. Fallon, V. Faka, M. A. Lange, M. A. Kraft, E. Suard, E. T. Connolly, B. E. Francisco, A. G. Squires and W. G. Zeier, *J. Am. Chem. Soc.*, 2025, **147**, 10151–10159.
24 J. Lee, S. Ju, S. Hwang, J. You, J. Jung, Y. Kang and S. Han, *ACS Appl. Mater. Interfaces*, 2024, **16**, 46442–46453.
25 M. Jang, K. Park, H.-G. Jung, K. Y. Chung, J. H. Shim, O. Kwon and S. Yu, *J. Mater. Chem. A*, 2025, **13**, 16547–16555.
26 D. Lu, H. Wang, M. Chen, L. Lin, R. Car, W. E, W. Jia and L. Zhang, *Comput. Phys. Commun.*, 2021, **259**, 107624.
27 C. Wang, K. Fu, S. P. Kammampata, D. W. McOwen, A. J. Samson, L. Zhang, G. T. Hitz, A. M. Nolan, E. D. Wachsman, Y. Mo, V. Thangadurai and L. Hu, *Chem. Rev.*, 2020, **120**, 4257–4300.
28 R. Zhao, G. Hu, S. Kmiec, J. Wheaton, V. M. Torres and S. W. Martin, *Batteries Supercaps*, 2022, **5**, e202100356.
29 S. W. Martin, *Handbook of Solid State Batteries*, 2016, pp. 433–501.
30 C. J. Leo, B. V. R. Chowdari, G. V. S. Rao and J. L. Souquet, *Mater. Res. Bull.*, 2002, **37**, 1419–1430.
31 A. Hayashi, Y. Ishikawa, S. Hama, T. Minami and M. Tatsumisago, *Electrochem. Solid-State Lett.*, 2003, **6**, A47–A49.
32 J. Yang, J. Lin, T. Brezesinski and F. Strauss, *ACS Energy Lett.*, 2024, **9**, 5977–5990.
33 Y. Seino, T. Ota, K. Takada, A. Hayashi and M. Tatsumisago, *Energy Environ. Sci.*, 2014, **7**, 627–631.
34 K. Sau, S. Takagi, T. Ikeshoji, K. Kisu, R. Sato, E. C. Dos Santos, H. Li, R. Mohtadi and S. Orimo, *Commun. Mater.*, 2024, **5**, 122.
35 J. Wolfenstine, J. L. Allen, J. Sakamoto, D. J. Siegel and H. Choe, *Ionics*, 2018, **24**, 1271–1276.
36 Q. Zhang, D. Cao, Y. Ma, A. Natan, P. Aurora and H. Zhu, *Adv. Mater.*, 2019, **31**, 1901131.
37 H. Liu, Y. Liang, C. Wang, D. Li, X. Yan, C. Nan and L. Fan, *Adv. Mater.*, 2023, **35**, 2206013.
38 X. Li, J. Liang, X. Yang, K. R. Adair, C. Wang, F. Zhao and X. Sun, *Energy Environ. Sci.*, 2020, **13**, 1429–1461.
39 Z. Cheng, W. Zhao, Q. Wang, C. Zhao, A. K. Lavrinenko, A. Vasileiadis, V. Landgraf, L. Bannenberg, Y. Li, J. Liang, M. Liu, S. Ganapathy and M. Wagemaker, *Nat. Mater.*, 2025, DOI: **10.1038/s41563-025-02296-6**.
40 Y.-C. Yin, J.-T. Yang, J.-D. Luo, G.-X. Lu, Z. Huang, J.-P. Wang, P. Li, F. Li, Y.-C. Wu, T. Tian, Y.-F. Meng, H.-S. Mo, Y.-H. Song, J.-N. Yang, L.-Z. Feng, T. Ma, W. Wen, K. Gong, L.-J. Wang, H.-X. Ju, Y. Xiao, Z. Li, X. Tao and H.-B. Yao, *Nature*, 2023, **616**, 77–83.
41 T.-T. Le, M. Abbas, D. M. Dreistadt, T. Klassen and C. Pistidda, *Chem. Eng. J.*, 2023, **473**, 145315.
42 R. Murugan, V. Thangadurai and W. Weppner, *Angew. Chem., Int. Ed.*, 2007, **46**, 7778–7781.
43 J. Awaka, N. Kijima, H. Hayakawa and J. Akimoto, *J. Solid State Chem.*, 2009, **182**, 2046–2052.
44 M. Burbano, D. Carlier, F. Boucher, B. J. Morgan and M. Salanne, *Phys. Rev. Lett.*, 2016, **116**, 135901.
45 J. Lu and Y. Li, *J. Mater. Sci.: Mater. Electron.*, 2021, **32**, 9736–9754.
46 K.-Y. Yang, J.-W. Wang and K.-Z. Fung, *J. Alloys Compd.*, 2008, **458**, 415–424.
47 J. B. Goodenough, H. Y.-P. Hong and J. A. Kafalas, *Mater. Res. Bull.*, 1976, **11**, 203–220.
48 M. Monchak, T. Hupfer, A. Senyshyn, H. Boysen, D. Chernyshov, T. Hansen, K. G. Schell, E. C. Bucharsky, M. J. Hoffmann and H. Ehrenberg, *Inorg. Chem.*, 2016, **55**, 2941–2945.
49 Y. K. Shin, M. Y. Sengul, A. S. M. Jonayat, W. Lee, E. D. Gomez, C. A. Randall and A. C. T. van Duin, *Phys. Chem. Chem. Phys.*, 2018, **20**, 22134–22147.
50 K. Arbi, M. Hoelzel, A. Kuhn, F. García-Alvarado and J. Sanz, *Inorg. Chem.*, 2013, **52**, 9290–9296.
51 H. Y.-P. Hong, *Mater. Res. Bull.*, 1978, **13**, 117–124.
52 R. Kanno and M. Murayama, *J. Electrochem. Soc.*, 2001, **148**, A742.
53 R. Kanno, T. Hata, Y. Kawamoto and M. Irie, *Solid State Ionics*, 2000, **130**, 97–104.
54 N. Kamaya, K. Homma, Y. Yamakawa, M. Hirayama, R. Kanno, M. Yonemura, T. Kamiyama, Y. Kato, S. Hama, K. Kawamoto and A. Mitsui, *Nat. Mater.*, 2011, **10**, 682–686.
55 B. Tao, C. Ren, H. Li, B. Liu, X. Jia, X. Dong, S. Zhang and H. Chang, *Adv. Funct. Mater.*, 2022, **32**, 2203551.
56 P. Bron, S. Johansson, K. Zick, J. Schmedt Auf Der Günne, S. Dehnen and B. Roling, *J. Am. Chem. Soc.*, 2013, **135**, 15694–15697.
57 D. A. Weber, A. Senyshyn, K. S. Weldert, S. Wenzel, W. Zhang, R. Kaiser, S. Berendts, J. Janek and W. G. Zeier, *Chem. Mater.*, 2016, **28**, 5905–5915.
58 S. T. Kong, Ö. Gün, B. Koch, H. J. Deiseroth, H. Eckert and C. Reiner, *Chem. – Eur. J.*, 2010, **16**, 5138–5147.
59 H. Deiseroth, S. Kong, H. Eckert, J. Vannahme, C. Reiner, T. Zaiß and M. Schlosser, *Angew. Chem., Int. Ed.*, 2008, **47**, 755–758.
60 Z. Zhang, Y. Sun, X. Duan, L. Peng, H. Jia, Y. Zhang, B. Shan and J. Xie, *J. Mater. Chem. A*, 2019, **7**, 2717–2722.
61 Y. Ou, Y. Ikeda, L. Scholz, S. Divinski, F. Fritzen and B. Grabowski, *Phys. Rev. Mater.*, 2024, **8**, 115407.
62 P. Adeli, J. D. Bazak, K. H. Park, I. Kochetkov, A. Huq, G. R. Goward and L. F. Nazar, *Angew. Chem., Int. Ed.*, 2019, **58**, 8681–8686.
63 J. Chen, M. Fang, Q. Wu, S. Tang, J. Zheng, C. Wei, X. Cao, Y. Shi, N. Xu and Y. He, *Chem. Mater.*, 2025, **37**, 591–599.
64 L. Hu, J. Wang, K. Wang, Z. Gu, Z. Xi, H. Li, F. Chen, Y. Wang, Z. Li and C. Ma, *Nat. Commun.*, 2023, **14**, 3807.
65 Y. Tanaka, K. Ueno, K. Mizuno, K. Takeuchi, T. Asano and A. Sakai, *Angew. Chem., Int. Ed.*, 2023, **135**, e202217581.
66 T. Zhao, B. Samanta, X. M. De Irujo-Labalde, G. Whang, N. Yadav, M. A. Kraft, P. Adelhelm, M. R. Hansen and W. G. Zeier, *ACS Mater. Lett.*, 2024, **6**, 3683–3689.
67 J. A. Newnham, J. Kondek, J. Hartel, C. Rosenbach, C. Li, V. Faka, L. Gronych, D. Glikman, F. Schreiner, D. D. Wind, B. Braunschweig, M. R. Hansen and W. G. Zeier, *Chem. Mater.*, 2025, **37**, 4130–4144.
68 S. Adams, *Energy Storage Mater.*, 2024, **68**, 103359.
69 B. Singh, Y. Wang, J. Liu, J. D. Bazak, A. Shyamsunder and L. F. Nazar, *J. Am. Chem. Soc.*, 2024, **146**, 17158–17169.
70 L. Duchêne, S. Lunghammer, T. Burankova, W.-C. Liao, J. P. Embs, C. Copéret, H. M. R. Wilkening, A. Remhof, H. Hagemann and C. Battaglia, *Chem. Mater.*, 2019, **31**, 3449–3460.
71 W. S. Tang, M. Matsuo, H. Wu, V. Stavila, A. Unemoto, S. Orimo and T. J. Udovic, *Energy Storage Mater.*, 2016, **4**, 79–83.
72 M. Brighi, F. Murgia and R. Černý, *Cell Rep. Phys. Sci.*, 2020, **1**, 100217.
73 S. Kalnaus, N. J. Dudney, A. S. Westover, E. Herbert and S. Hackney, *Science*, 2023, **381**, eabg5998.
74 E. Milan and M. Pasta, *Mater. Futures*, 2023, **2**, 013501.

75 A. Hayashi, S. Hama, H. Morimoto, M. Tatsumisago and T. Minami, *J. Am. Ceram. Soc.*, 2004, **84**, 477–479.
76 J. Zhang, C. Gao, C. He, L. Tan, S. Kang, Q. Jiao, T. Xu and C. Lin, *J. Am. Ceram. Soc.*, 2023, **106**, 354–364.
77 S. Ujiie, A. Hayashi and M. Tatsumisago, *Solid State Ionics*, 2012, **211**, 42–45.
78 R. Zhao, G. Hu, S. Kmiec, R. Gebhardt, A. Whale, J. Wheaton and S. W. Martin, *ACS Appl. Mater. Interfaces*, 2021, **13**, 26841–26852.
79 J. B. Bates, N. J. Dudney, G. R. Gruzalski, R. A. Zuhr, A. Choudhury, C. F. Luck and J. D. Robertson, *J. Power Sources*, 1993, **43**, 103–110.
80 W. Wang, X. Yue, J. Meng, J. Wang, X. Wang, H. Chen, D. Shi, J. Fu, Y. Zhou, J. Chen and Z. Fu, *Energy Storage Mater.*, 2019, **18**, 414–422.
81 S. Zhang, F. Zhao, L.-Y. Chang, Y.-C. Chuang, Z. Zhang, Y. Zhu, X. Hao, J. Fu, J. Chen, J. Luo, M. Li, Y. Gao, Y. Huang, T.-K. Sham, M. D. Gu, Y. Zhang, G. King and X. Sun, *J. Am. Chem. Soc.*, 2024, **146**, 2977–2985.
82 L. Qian, S. Tu, Y. Wang, X. Yang, C. Ye and S.-Z. Qiao, *J. Am. Chem. Soc.*, 2025, **147**, 23170–23179.
83 H. Duan, C. Wang, X.-S. Zhang, J. Fu, W. Li, J. Wan, R. Yu, M. Fan, F. Ren, S. Wang, M. Zheng, X. Li, J. Liang, R. Wen, S. Xin, Y.-G. Guo and X. Sun, *J. Am. Chem. Soc.*, 2024, **146**, 29335–29343.
84 M. H. Braga, J. A. Ferreira, V. Stockhausen, J. E. Oliveira and A. El-Azab, *J. Mater. Chem. A*, 2014, **2**, 5470–5480.
85 I. You, B. Singh, M. Cui, G. Goward, L. Qian, Z. Arthur, G. King and L. F. Nazar, *Energy Environ. Sci.*, 2025, **18**, 478–491.
86 T. Dai, S. Wu, Y. Lu, Y. Yang, Y. Liu, C. Chang, X. Rong, R. Xiao, J. Zhao, Y. Liu, W. Wang, L. Chen and Y.-S. Hu, *Nat. Energy*, 2023, **8**, 1221–1228.
87 Q. Yang, J. Xu, X. Fu, J. Lian, L. Wang, X. Gong, R. Xiao and H. Li, *J. Mater. Chem. A*, 2025, **13**, 2309–2315.
88 M. Kulichenko, B. Nebgen, N. Lubbers, J. S. Smith, K. Barros, A. E. A. Allen, A. Habib, E. Shinkle, N. Fedik, Y. W. Li, R. A. Messerly and S. Tretiak, *Chem. Rev.*, 2024, **124**, 13681–13714.
89 J. Behler and M. Parrinello, *Phys. Rev. Lett.*, 2007, **98**, 146401.
90 S. Chmiela, H. E. Sauceda, I. Poltavsky, K.-R. Müller and A. Tkatchenko, *Comput. Phys. Commun.*, 2019, **240**, 38–45.
91 A. P. Bartók, M. C. Payne, R. Kondor and G. Csányi, *Phys. Rev. Lett.*, 2010, **104**, 136403.
92 K. Miwa and H. Ohno, *Phys. Rev. Mater.*, 2017, **1**, 053801.
93 R. Jinnouchi, F. Karsai and G. Kresse, *Phys. Rev. B*, 2019, **100**, 014105.
94 R. Jinnouchi, J. Lahnsteiner, F. Karsai, G. Kresse and M. Bokdam, *Phys. Rev. Lett.*, 2019, **122**, 225701.
95 A. V. Shapeev, *Multiscale Model. Simul.*, 2016, **14**, 1153–1173.
96 L. Zhang, J. Han, H. Wang, W. Saidi, R. Car and W. E, in *Advances in neural information processing systems 31*, ed. S. Bengio, H. Wallach, H. Larochelle, K. Grauman, N. Cesa-Bianchi and R. Garnett, Curran Associates, Inc., 2018, pp. 4436–4446.
97 L. Zhang, J. Han, H. Wang, R. Car and W. E, *Phys. Rev. Lett.*, 2018, **120**, 143001.
98 N. Artrith and A. Urban, *Comput. Mater. Sci.*, 2016, **114**, 135–150.
99 A. Singraber, T. Morawietz, J. Behler and C. Dellago, *J. Chem. Theory Comput.*, 2019, **15**, 3075–3092.
100 A. Khorshidi and A. A. Peterson, *Comput. Phys. Commun.*, 2016, **207**, 310–324.
101 K. Lee, D. Yoo, W. Jeong and S. Han, *Comput. Phys. Commun.*, 2019, **242**, 95–103.
102 X. Wang, Y. Wang, L. Zhang, F. Dai and H. Wang, *Nucl. Fusion*, 2022, **62**, 126013.
103 D. Zhang, H. Bi, F.-Z. Dai, W. Jiang, X. Liu, L. Zhang and H. Wang, *npj Comput. Mater.*, 2024, **10**, 94.
104 D. Zhang, X. Liu, X. Zhang, C. Zhang, C. Cai, H. Bi, Y. Du, X. Qin, A. Peng, J. Huang, B. Li, Y. Shan, J. Zeng, Y. Zhang, S. Liu, Y. Li, J. Chang, X. Wang, S. Zhou, J. Liu, X. Luo, Z. Wang, W. Jiang, J. Wu, Y. Yang, J. Yang, M. Yang, F.-Q. Gong, L. Zhang, M. Shi, F.-Z. Dai, D. M. York, S. Liu, T. Zhu, Z. Zhong, J. Lv, J. Cheng, W. Jia, M. Chen, G. Ke, W. E, L. Zhang and H. Wang, *npj Comput. Mater.*, 2024, **10**, 293.
105 Z. Fan, Y. Wang, P. Ying, K. Song, J. Wang, Y. Wang, Z. Zeng, K. Xu, E. Lindgren, J. M. Rahm, A. J. Gabourie, J. Liu, H. Dong, J. Wu, Y. Chen, Z. Zhong, J. Sun, P. Erhart, Y. Su and T. Ala-Nissila, *J. Chem. Phys.*, 2022, **157**, 114801.
106 K. Song, R. Zhao, J. Liu, Y. Wang, E. Lindgren, Y. Wang, S. Chen, K. Xu, T. Liang, P. Ying, N. Xu, Z. Zhao, J. Shi, J. Wang, S. Lyu, Z. Zeng, S. Liang, H. Dong, L. Sun, Y. Chen, Z. Zhang, W. Guo, P. Qian, J. Sun, P. Erhart, T. Ala-Nissila, Y. Su and Z. Fan, *Nat. Commun.*, 2024, **15**, 10208.
107 I. Batatia, D. P. Kovács, G. N. C. Simm, C. Ortner and G. Csányi, *arXiv*, 2023, preprint, arXiv:2206.07697, DOI: 10.48550/arXiv.2206.07697.
108 S. Batzner, A. Musaelian, L. Sun, M. Geiger, J. P. Mailoa, M. Kornbluth, N. Molinari, T. E. Smidt and B. Kozinsky, *Nat. Commun.*, 2022, **13**, 2453.
109 D. Zhang, A. Peng, C. Cai, W. Li, Y. Zhou, J. Zeng, M. Guo, C. Zhang, B. Li, H. Jiang, T. Zhu, W. Jia, L. Zhang and H. Wang, 2025.
110 B. Deng, P. Zhong, K. Jun, J. Riebesell, K. Han, C. J. Bartel and G. Ceder, *Nat Mach Intell*, 2023, **5**, 1031–1041.
111 V. L. Deringer, M. A. Caro and G. Csányi, *Adv. Mater.*, 2019, **31**, 1902765.
112 A. P. Bartók, R. Kondor and G. Csányi, *Phys. Rev. B*, 2013, **87**, 184115.
113 V. L. Deringer and G. Csányi, *Phys. Rev. B*, 2017, **95**, 094203.
114 Y. Zuo, C. Chen, X. Li, Z. Deng, Y. Chen, J. Behler, G. Csányi, A. V. Shapeev, A. P. Thompson, M. A. Wood and S. P. Ong, *J. Phys. Chem. A*, 2020, **124**, 731–745.
115 R. Drautz, *Phys. Rev. B*, 2019, **99**, 014104.
116 Y. Lysogorskiy, C. V. D. Oord, A. Bochkarev, S. Menon, M. Rinaldi, T. Hammerschmidt, M. Mrovec, A. Thompson, G. Csányi, C. Ortner and R. Drautz, *npj Comput. Mater.*, 2021, **7**, 97.
117 A. P. Thompson, L. P. Swiler, C. R. Trott, S. M. Foiles and G. J. Tucker, *J. Comput. Phys.*, 2015, **285**, 316–330.
118 N. Thomas, T. Smidt, S. Kearnes, L. Yang, L. Li, K. Kohlhoff and P. Riley, 2018.
119 M. Geiger and T. Smidt, *arXiv*, 2022, preprint, arXiv:2207.09453, DOI: 10.48550/arXiv.2207.09453.
120 J. Zeng, D. Zhang, A. Peng, X. Zhang, S. He, Y. Wang, X. Liu, H. Bi, Y. Li, C. Cai, C. Zhang, Y. Du, J.-X. Zhu, P. Mo, Z. Huang, Q. Zeng, S. Shi, X. Qin, Z. Yu, C. Luo, Y. Ding, Y.-P. Liu, R. Shi, Z. Wang, S. L. Bore, J. Chang, Z. Deng, Z. Ding, S. Han, W. Jiang, G. Ke, Z. Liu, D. Lu, K. Muraoka, H. Oliaei, A. K. Singh, H. Que, W. Xu, Z. Xu, Y.-B. Zhuang, J. Dai, T. J. Giese, W. Jia, B. Xu, D. M. York, L. Zhang and H. Wang, *J. Chem. Theory Comput.*, 2025, **21**, 4375–4385.
121 A. Musaelian, S. Batzner, A. Johansson, L. Sun, C. J. Owen, M. Kornbluth and B. Kozinsky, *arXiv*, 2022, preprint, arXiv:2204.05249, DOI: 10.48550/arXiv.2204.05249.
122 V. Bharadwaj, A. Glover, A. Buluc and J. Demmel, in SIAM conference on applied and computational discrete algorithms (ACDA25), Society for Industrial and Applied Mathematics, 2025.
123 B. Cheng, *npj Comput. Mater.*, 2024, **10**, 157.
124 M. Wen, W.-F. Huang, J. Dai and S. Adhikari, *npj Comput. Mater.*, 2025, **11**, 128.
125 D. Bayerl, C. M. Andolina, S. Dwaraknath and W. A. Saidi, *Digital Discovery*, 2022, **1**, 61–69.
126 J. S. Smith, B. Nebgen, N. Lubbers, O. Isayev and A. E. Roitberg, *J. Chem. Phys.*, 2018, **148**, 241733.
127 I. S. Novikov, K. Gubaev, E. V. Podryabinkin and A. V. Shapeev, *Mach. Learn.: Sci. Technol.*, 2021, **2**, 025002.
128 Y. Zhang, H. Wang, W. Chen, J. Zeng, L. Zhang, H. Wang and W. E, *Comput. Phys. Commun.*, 2020, **253**, 107206.
129 C. Van Der Oord, M. Sachs, D. P. Kovács, C. Ortner and G. Csányi, *npj Comput. Mater.*, 2023, **9**, 168.
130 Y. Wang, K. Takaba, M. S. Chen, M. Wieder, Y. Xu, T. Zhu, J. Z. H. Zhang, A. Nagle, K. Yu, X. Wang, D. J. Cole, J. A. Rackers, K. Cho, J. G. Greener, P. Eastman, S. Martiniani and M. E. Tuckerman, *Appl. Phys. Rev.*, 2025, **12**, 021304.
131 A. R. Tan, S. Urata, S. Goldman, J. C. B. Dietschreit and R. Gómez-Bombarelli, *npj Comput. Mater.*, 2023, **9**, 225.
132 J. Qi, S. Banerjee, Y. Zuo, C. Chen, Z. Zhu, M. L. Holekevi Chandrappa, X. Li and S. P. Ong, *Mater. Today Phys.*, 2021, **21**, 100463.
133 Z. Xu, H. Duan, Z. Dou, M. Zheng, Y. Lin, Y. Xia, H. Zhao and Y. Xia, *npj Comput. Mater.*, 2023, **9**, 105.
134 L. Gigli, D. Tisi, F. Grasselli and M. Ceriotti, *Chem. Mater.*, 2024, **36**, 1482–1496.
135 K. Shimizu, P. Bahuguna, S. Mori, A. Hayashi and S. Watanabe, *J. Phys. Chem. C*, 2024, **128**, 10139–10145.

136 H. Yamada, K. Ohara, S. Hiroi, A. Sakuda, K. Ikeda, T. Ohkubo, K. Nakada, H. Tsukasaki, H. Nakajima, L. Temleitner, L. Pusztai, S. Ariga, A. Matsuo, J. Ding, T. Nakano, T. Kimura, R. Kobayashi, T. Usuki, S. Tahara, K. Amezawa, Y. Tateyama, S. Mori and A. Hayashi, *Energy Environ. Mater.*, 2024, **7**, e12612.
137 R. Zhou, K. Luo, S. W. Martin and Q. An, *ACS Appl. Mater. Interfaces*, 2024, **16**, 18874–18887.
138 C. Wang, M. Aykol and T. Mueller, *Chem. Mater.*, 2023, **35**, 6346–6356.
139 L. Bekaert, S. Akatsuka, N. Tanibata, F. De Proft, A. Hubin, M. H. Mamme and M. Nakayama, *J. Phys. Chem. C*, 2023, **127**, 8503–8514.
140 M. K. Gupta, J. Ding, N. C. Osti, D. L. Abernathy, W. Arnold, H. Wang, Z. Hood and O. Delaire, *Energy Environ. Sci.*, 2021, **14**, 6554–6563.
141 M. Bertani and A. Pedone, *J. Phys. Chem. C*, 2025, **129**, 12697–12709.
142 K. Luo, R. Zhou, S. W. Martin and Q. An, *J. Mater. Chem. A*, 2024, **12**, 33518–33525.
143 J. Klarbring and A. Walsh, *Chem. Mater.*, 2024, **36**, 9406–9413.
144 G. Winter and R. Gómez-Bombarelli, *J. Phys. Energy*, 2023, **5**, 024004.
145 J. Huang, L. Zhang, H. Wang, J. Zhao, J. Cheng and W. E, *J. Chem. Phys.*, 2021, **154**, 094703.
146 K. Kim, A. Dive, A. Grieder, N. Adelstein, S. Kang, L. F. Wan and B. C. Wood, *J. Chem. Phys.*, 2022, **156**, 221101.
147 Z. Yan and Y. Zhu, *Chem. Mater.*, 2024, **36**, 11551–11557.
148 D. Zhang, Y. You, F. Wu, X. Cao, T.-Y. Lü, Y. Sun, Z.-Z. Zhu and S. Wu, *ACS Mater. Lett.*, 2024, **6**, 1849–1855.
149 K. Miwa and R. Asahi, *Phys. Rev. Mater.*, 2018, **2**, 105404.
150 D. Sun, N. Wu, Y. Wen, S. Sun, Y. He, K. Huang, C. Li, B. Ouyang, R. White and K. Huang, *J. Mater. Chem. A*, 2025, **13**, 10224–10231.
151 I. A. Balyakin, M. I. Vlasov, S. V. Pershina, D. M. Tsymbarenko and A. A. Rempel, *Comput. Mater. Sci.*, 2024, **239**, 112979.
152 A. D. Dembitskiy, S. N. Marshenya, E. V. Antipov, S. S. Fedotov and D. A. Aksyonov, *J. Power Sources*, 2025, **642**, 236979.
153 G. Chaney, A. Golov, A. Van Roekeghem, J. Carrasco and N. Mingo, *ACS Appl. Mater. Interfaces*, 2024, **16**, 24624–24630.
154 G. Lai, R. Zhang, C. Fang, J. Zhao, T. Chen, Y. Zuo, B. Xu and J. Zheng, *npj Comput. Mater.*, 2025, **11**, 245.
155 J. H. Kim, B. Jun, Y. J. Jang, S. H. Choi, S. H. Choi, S. M. Cho, Y.-G. Kim, B.-H. Kim and S. U. Lee, *Nano Energy*, 2024, **124**, 109436.
156 Z. Li, X. Ren, J. Li, R. Xiao and H. Li, *ACS Appl. Energy Mater.*, 2025, **8**, 11011–11020.
157 R. Li, K. Xu, S. Wen, X. Tang, Z. Lin, X. Guo, M. Avdeev, Z. Zhang and Y.-S. Hu, *Nat. Commun.*, 2025, **16**, 6633.
158 M. Lei, B. Li, R. Yin, X. D. Ji and D. Jiang, *Adv. Funct. Mater.*, 2024, **34**, 2410509.
159 A. P. Maltsev, I. V. Chepkasov and A. R. Oganov, *ACS Appl. Mater. Interfaces*, 2023, **15**, 42511–42519.
160 Z. Xu, Y. Lin, Y. Xia, Y. Jiang, X. Feng, Z. Liu, L. Shen, M. Zheng and Y. Xia, *J. Power Sources*, 2025, **637**, 236591.
161 R. Zhou, K. Luo, L. Fei and Q. An, *ACS Electrochem.*, 2025, **1**, 143–152.
162 Z. Deng, C. Chen, X.-G. Li and S. P. Ong, *arXiv*, 2019, preprint, arXiv:1901.08749 [cond-mat], DOI: **10.48550/arXiv.1901.08749**.
163 G. Krenzer, J. Klarbring, K. Tolborg, H. Rossignol, A. R. McCluskey, B. J. Morgan and A. Walsh, *Chem. Mater.*, 2023, **35**, 6133–6140.
164 A. P. Maltsev, I. V. Chepkasov, A. G. Kvashnin and A. R. Oganov, *Crystals*, 2023, **13**, 756.
165 A. Seth, R. P. Kulkarni and G. Sai Gautam, *ACS Mater. Au*, 2025, **5**, 458–468.
166 K. Mori, K. Iwase, Y. Oba, K. Ikeda, T. Otomo and T. Fukunaga, *Solid State Ionics*, 2020, **344**, 115141.
167 K. Ohara, A. Mitsui, M. Mori, Y. Onodera, S. Shiotani, Y. Koyama, Y. Orikasa, M. Murakami, K. Shimoda, K. Mori, T. Fukunaga, H. Arai, Y. Uchimoto and Z. Ogumi, *Sci. Rep.*, 2016, **6**, 21302.
168 Z. Xu and Y. Xia, *J. Mater. Chem. A*, 2022, **10**, 11854–11880.
169 M. Sadowski and K. Albe, *J. Power Sources*, 2020, **478**, 229041.
170 C. Liu, Z. Zhang, J. Ding and E. Ma, *Scr. Mater.*, 2023, **225**, 115159.
171 P. Cuillier, M. G. Tucker and Y. Zhang, *J. Appl. Crystallogr.*, 2024, **57**, 1780–1788.
172 M. Lei, B. Li, H. Liu and D. Jiang, *Angew. Chem., Int. Ed.*, 2024, **63**, e202315628.
173 T. J. Udovic, M. Matsuo, W. S. Tang, H. Wu, V. Stavila, A. V. Soloninin, R. V. Skoryunov, O. A. Babanova, A. V. Skripov, J. J. Rush, A. Unemoto, H. Takamura and S. Orimo, *Adv. Mater.*, 2014, **26**, 7622–7626.
174 A. P. Maltsev, I. V. Chepkasov and A. R. Oganov, *ACS Appl. Mater. Interfaces*, 2023, **15**, 42511–42519.
175 W. S. Tang, M. Matsuo, H. Wu, V. Stavila, W. Zhou, A. A. Talin, A. V. Soloninin, R. V. Skoryunov, O. A. Babanova, A. V. Skripov, A. Unemoto, S. Orimo and T. J. Udovic, *Adv. Energy Mater.*, 2016, **6**, 1502237.
176 S. Wang, Y. Liu and Y. Mo, *Angew. Chem., Int. Ed.*, 2023, **62**, e202215544.
177 X. He, Y. Zhu, A. Epstein and Y. Mo, *npj Comput. Mater.*, 2018, **4**, 18.
178 K. Jun, B. Lee, R. L. Kam and G. Ceder, *Proc. Natl. Acad. Sci. U. S. A.*, 2024, **121**, e2316493121.
179 J. G. Smith and D. J. Siegel, *Nat. Commun.*, 2020, **11**, 1483.
180 Z. Zhang, H. Li, K. Kaup, L. Zhou, P.-N. Roy and L. F. Nazar, *Matter*, 2020, **2**, 1667–1684.
181 N. Verdal, T. J. Udovic, J. J. Rush, R. L. Cappelletti and W. Zhou, *J. Phys. Chem. A*, 2011, **115**, 2933–2938.
182 N. Verdal, T. J. Udovic, V. Stavila, W. S. Tang, J. J. Rush and A. V. Skripov, *J. Phys. Chem. C*, 2014, **118**, 17483–17489.
183 K. Sau, T. Ikeshoji, S. Kim, S. Takagi and S. Orimo, *Chem. Mater.*, 2021, **33**, 2357–2369.
184 A. V. Skripov, O. A. Babanova, A. V. Soloninin, V. Stavila, N. Verdal, T. J. Udovic and J. J. Rush, *J. Phys. Chem. C*, 2013, **117**, 25961–25968.
185 K. Sau, T. Ikeshoji, S. Kim, S. Takagi, K. Akagi and S. Orimo, *Phys. Rev. Mater.*, 2019, **3**, 075402.
186 Y. You, D. Zhang, Z. Wu, T.-Y. Lü, X. Cao, Y. Sun, Z.-Z. Zhu and S. Wu, *Nat. Commun.*, 2025, **16**, 4630.
187 W. Li, J. A. Quirk, M. Li, W. Xia, L. M. Morgan, W. Yin, M. Zheng, L. C. Gallington, Y. Ren, N. Zhu, G. King, R. Feng, R. Li, J. A. Dawson, T. Sham and X. Sun, *Adv. Mater.*, 2024, **36**, 2302647.
188 F. Ren, Y. Wu, W. Zuo, W. Zhao, S. Pan, H. Lin, H. Yu, J. Lin, M. Lin, X. Yao, T. Brezesinski, Z. Gong and Y. Yang, *Energy Environ. Sci.*, 2024, **17**, 2743–2752.
189 T. Hu, H. Huang, G. Zhou, X. Wang, J. Zhu, Z. Cheng, F. Fu, X. Wang, F. Dai, K. Yu and S. Xu, *Nat. Commun.*, 2025, **16**, 7379.
190 A. K. Rappe and W. A. I. Goddard, *J. Phys. Chem.*, 1991, **95**, 3358–3363.
191 E. Podryabinkin, K. Garifullin, A. Shapeev and I. Novikov, *J. Chem. Phys.*, 2023, **159**, 084112.
192 S. P. Niblett, P. Kourtis, I.-B. Magdău, C. P. Grey and G. Csányi, *J. Chem. Theory Comput.*, 2025, **21**, 6096–6112.
193 R. Wang, M. Guo, Y. Gao, X. Wang, Y. Zhang, B. Deng, X. Chen, M. Shi, L. Zhang and Z. Zhong, 2024.
194 I. Batatia, P. Benner, Y. Chiang, A. M. Elena, D. P. Kovács, J. Riebesell, X. R. Advincula, M. Asta, W. J. Baldwin, N. Bernstein, A. Bhowmik, S. M. Blau, V. Cărare, J. P. Darby, S. De, F. D. Pia, V. L. Deringer, R. Elijošius, Z. El-Machachi, E. Fako, A. C. Ferrari, A. Genreith-Schriever, J. George, R. E. A. Goodall, C. P. Grey, S. Han, W. Handley, H. H. Heenen, K. Hermansson, C. Holm, J. Jaafar, S. Hofmann, K. S. Jakob, H. Jung, V. Kapil, A. D. Kaplan, N. Karimitari, N. Kroupa, J. Kullgren, M. C. Kuner, D. Kuryla, G. Liepuoniute, J. T. Margraf, I.-B. Magdău, A. Michaelides, J. H. Moore, A. A. Naik, S. P. Niblett, S. W. Norwood, N. O'Neill, C. Ortner, K. A. Persson, K. Reuter, A. S. Rosen, L. L. Schaaf, C. Schran, E. Sivonxay, T. K. Stenczel, V. Svahn, C. Sutton, C. van der Oord, E. Varga-Umbrich, T. Vegge, M. Vondrák, Y. Wang, W. C. Witt, F. Zills and G. Csányi.
195 R. Jacobs, D. Morgan, S. Attarian, J. Meng, C. Shen, Z. Wu, C. Y. Xie, J. H. Yang, N. Artrith, B. Blaiszik, G. Ceder, K. Choudhary, G. Csanyi, E. D. Cubuk, B. Deng, R. Drautz, X. Fu, J. Godwin, V. Honavar, O. Isayev, A. Johansson, B. Kozinsky, S. Martiniani, S. P. Ong, I. Poltavsky, K. Schmidt, S. Takamoto, A. P. Thompson, J. Westermayr and B. M. Wood, *Curr. Opin. Solid State Mater. Sci.*, 2025, **35**, 101214.
196 M. Radova, W. G. Stark, C. S. Allen, R. J. Maurer and A. P. Bartók, *npj Comput. Mater.*, 2025, **11**, 237.
197 T. Yang, Z. Cai, Z. Huang, W. Tang, R. Shi, A. Godfrey, H. Liu, Y. Lin, C.-W. Nan, M. Ye, L. Zhang, K. Wang, H. Wang and B. Xu, *Phys. Rev. B*, 2024, **110**, 064427.

198 E. Watanabe, W. Zhao, A. Sugahara, B. Mortemard de Boisse, L. Lander, D. Asakura, Y. Okamoto, T. Mizokawa, M. Okubo and A. Yamada, *Chem. Mater.*, 2019, **31**, 2358–2365.
199 H. Gao, X. Ai, H. Wang, W. Li, P. Wei, Y. Cheng, S. Gui, H. Yang, Y. Yang and M.-S. Wang, *Nat. Commun.*, 2022, **13**, 5050.
200 T. W. Ko, J. A. Finkler, S. Goedecker and J. Behler, *Nat. Commun.*, 2021, **12**, 398.
201 L. Zhang, H. Wang, M. C. Muniz, A. Z. Panagiotopoulos, R. Car and W. E, *J. Chem. Phys.*, 2022, **156**, 124107.
202 B. Cheng, *npj Comput. Mater.*, 2025, **11**, 80.
203 A. Kutana, K. Shimizu, S. Watanabe and R. Asahi, *Sci. Rep.*, 2025, **15**, 16719.
204 P. Zhong, D. Kim, D. S. King and B. Cheng, *arXiv*, 2025, preprint, arXiv:2504.05169, DOI: **10.48550/arXiv.2504.05169**.